Published in final edited form as:
Biomaterials. 2015 January ; 37: 25–39. doi:10.1016/j.biomaterials.2014.10.040.

Mechanical failure modes of chronically implanted planar silicon-based neural probes for laminar recording

Takashi D. Y. Kozai[1,2,3], **Kasey Catt**[1], **Xia Li**[1], **Zhannetta V. Gugel**[1,6], **Valur T. Olafsson**[4], **Alberto L. Vazquez**[1,5], and **X. Tracy Cui**[1,2,3]

[1]Department of Bioengineering, University of Pittsburgh, Pittsburgh, PA

[2]Center for Neural Basis of Cognition, Pittsburgh, PA

[3]McGowan Institute for Regenerative Medicine, Pittsburgh, PA

[4]Neuroscience Imaging Center, University of Pittsburgh, Pittsburgh, PA

[5]Department of Radiology, University of Pittsburgh, Pittsburgh, PA

[6]Division of Biology and Biological Engineering, California Institute of Technology

Abstract

Penetrating intracortical electrode arrays that record brain activity longitudinally are powerful tools for basic neuroscience research and emerging clinical applications. However, regardless of the technology used, signals recorded by these electrodes degrade over time. The failure mechanisms of these electrodes are understood to be a complex combination of the biological reactive tissue response and material failure of the device over time. While mechanical mismatch between the brain tissue and implanted neural electrodes have been studied as a source of chronic inflammation and performance degradation, the electrode failure caused by mechanical mismatch between different material properties and different structural components within a device have remained poorly characterized. Using Finite Element Model (FEM) we simulate the mechanical strain on a planar silicon electrode. The results presented here demonstrate that mechanical mismatch between iridium and silicon leads to concentrated strain along the border of the two materials. This strain is further focused on small protrusions such as the electrical traces in planar silicon electrodes. These findings are confirmed with chronic in vivo data (133–189 days) in mice by correlating a combination of single-unit electrophysiology, evoked multi-unit recordings, electrochemical impedance spectroscopy, and scanning electron microscopy from traces and electrode sites with our modeling data. Several modes of mechanical failure of chronically implanted planar silicon electrodes are found that result in degradation and/or loss of recording.

Corresponding authors: Takashi D.Y. Kozai, Ph.D., Department of Bioengineering, University of Pittsburgh, 5065 Biomedical Science Tower 3, 3501 Fifth Avenue, Pittsburgh, PA 15260, tdk18@pitt.edu, tkozai@umich.edu, X. Tracy Cui, Ph.D., Department of Bioengineering, University of Pittsburgh, 5057 Biomedical Science Tower 3, 3501 Fifth Avenue, Pittsburgh, PA 15260, Ph: 412-383-6672, Fx: 412-383-5918, xic11@pitt.edu.

These findings highlight the importance of strains and material properties of various subcomponents within an electrode array.

Keywords

Finite Element Modeling; Scanning Electron Microscopy; Mechanical Failure; Material Failure; Strain; Chronic; Intracortical Electrode; Neural Interface; Structural Failure; In Vivo; Magnetic Resonance Imaging; Impedance Spectroscopy; Abiotic Failure

2. Introduction

Chronically implanted intracortical electrode arrays are powerful research tools for understanding functions of the brain [1–11]. These tools are used for monitoring neural activity longitudinally to study memory, plasticity, and aging, and can be especially powerful when combined with emerging transgenic and *in vivo* imaging tools [12]. They have also demonstrated promising clinical use in allowing human patients with tetraplegia to control neuroprosthetic devices such as a robotic arm or computer cursors [13, 14]. While long-term neural implants have demonstrated feasibility [13–16], the large variability and poor longevity of the recorded signals have presented a major challenge [17–23]. Electrophysiology and histology results show significant differences in recording performance and tissue response with the same device across different animals, between different electrode shanks in the same animal, and at different depths on the same shank [18, 19, 24–29]. This performance variability and degradation are understood to be the result of a complex combination of biological and material failure mechanisms [20, 30].

Many recent studies have focused on understanding the biological sources of variability. During implant insertion, penetrating a single major intracortical blood vessel results in a significantly large area of bleeding and blood brain barrier (BBB) disruption when compared to penetrating through many small capillaries [17]. This bleeding damages the local tissue, diminishing recording performance [31]. It has also been shown that implanting electrodes closer to major penetrating blood vessels, without damaging them, leads to increased astroglial activity [32, 33]. Consequences of BBB damage are not limited to leakage, the loss of oxygen perfusion to the tissue near the probe can also lead to secondary metabolic injury [12]. In addition to the initial insertion injury [17, 34, 35], chronic presence of the implant may cause persistent BBB disruption, chronic inflammation, and neuronal degeneration, which may lead to long-term recording failure of the implanted electrodes [20, 36].

While biological tissue responses contribute to the recording variability and degradation, electrode material failure also plays a significant role. Currently, the most widely used and commercially available intracortical electrode arrays for chronic neural recordings include bed-of-needle type (eg. microwire arrays and bulk silicon micromachined Utah-arrays) [18, 37], and thin-film microfabricated planar arrays [38]. Several studies have characterized the material failure mechanism of microwire- and Utah- arrays [20, 39, 40]. Failure modes include corrosion, cracking, bending of recording sites, and delamination or cracking of the insulating polymer materials, such as parylene-C [20, 39, 40]. However, limited

investigation has been reported on the mechanical failure modes of thin film planar silicon arrays. These arrays can have multiple electrode sites located along the depth of the probe shanks, which allows for the simultaneous sampling of multiple cortical and subcortical layers necessary for many neural circuitry studies [1, 41–43]. Understanding the failure modes of these arrays will help identify limitations in research and applications as well as potential opportunities for design improvements.

One representative planar array that is commercially available and widely used is the silicon based Michigan probes. These electrodes are made on a degenerately Boron-doped silicon-on-insulator substrates (Fracture Strength: 1,800 MPa) [38, 44, 45]. An insulating layer of silicon oxide is deposited onto the substrate (Fracture Strength: 360 MPa) [46], which is followed by the deposition of conductive polycrystalline silicon (polysilicon) electrode traces (Fracture Strength: 1,200 MPa) [47]. The traces are then insulated with a layer of silicon oxide, or a multilayer silicon oxide; silicon nitride; silicon oxide film. Finally, the iridium recording site is sputter coated on the electrode contact pads (see [38, 44] for details) (Fracture Strength: 500–740 MPa) [48].

While chronically implanted planar silicon arrays are widely used in chronic rodent neuroscience studies [49–51], challenges have been reported in chronic primate applications [52, 53]. These issues are likely due to the increase in brain size, increased interstitial space in the skull for brain movement, and the consequent increase in force experienced by the probes. Finite Element Modeling (FEM) studies have explored the tissue strain resulting from the mechanical mismatch between the planar probe and tissue [54, 55]. It has also been shown that this mechanical mismatch in the brain changes over time [56]. However, the strain resulting from mechanical mismatch within a device has largely been ignored.

This study aims to understand the mechanical failure modes of silicon based planar electrode arrays. Here we employ FEM to examine the microstructures of the array that are vulnerable to mechanical strain. We show that the protruded electrode traces are focal points of induced mechanical strain, particularly around the edges of the iridium recording sites where mechanical strain is highest. The results are then validated by electrodes that were implanted in the visual cortex of mice for 4–6 months. Electrode performance degradation is assessed through impedance spectroscopy and neural recordings, which are correlated to visible polysilicon trace damage near the iridium recording site observed by scanning electron microscopy (SEM). Lastly, the interstitial space between the brain and skull are examined in human, primate, and rodent via MRI to estimate the extent of the mechanical failure with the scaling of animal size and provide insight towards future microelectrode design.

3. Methods

3.1. Finite-element model

A 3D finite-element model of a 15 μm thick, 123 μm wide planar silicon electrode was developed in ANSYS 14.5 (Canonsburg, PA) to examine von Mises Equivalent Elastic Strain using a model previously established [55]. Briefly, von Mises Equivalent Elastic Strain represents the effective strain on an object combined from three principal strains in

mutually perpendicular axes and best characterizes the total strain along the entire probe. This is represented in ANSYS by the formula;

$$\varepsilon_e = 1\frac{1}{1+\nu'}\sqrt{\frac{1}{2}[(\varepsilon_1-\varepsilon_2)^2+(\varepsilon_2-\varepsilon_3)^2+(\varepsilon_3-\varepsilon_1)^2]} \quad [1]$$

where ε_e represents the von Mises Equivalent Elastic Strain, *v'* is the effective Poisson's ratio, and ε_1, ε_2, and ε_3 represents the principal strains oriented to the three axes [57].

16 electrical traces were extruded 0.6 μm from the surface of the electrode with 2.5 μm trace width and 4 μm inter-trace spacing using the 'add material' feature. To simplify the model, the polysilicon traces, silicon oxide or silicon oxide/silicon nitride insulation were modeled with the same material properties as bulk silicon (Young's modulus of 200 GPa and Poisson's ratio of 0.278) used in a previously published model [55]. It is estimated that this model will be a conservative evaluation as polysilicon, silicon oxide, and silicon nitride are considered to be more brittle than the bulk silicon.

To model 703 μm^2 single shank Michigan electrodes, 16 iridium (Ir) recording sites with 30 μm diameter were protruded 1500 Å from the traces using the 'add frozen' operation. Ir material properties were imported from the default ANSYS Engineering Data Library (Young's modulus of 528 GPa and Poisson's ratio of 0.26) [58]. The recording sites and substrate/trace parts were combined into one body. This simplifies the model by assuming that the recording sites will not delaminate from the substrate.

Again, using the previously published model, a 1.4 mm × 1.4 mm × 2.0 mm cube at 37°C was used to model the brain (Young's modulus of 6 kPa and Poisson's ratio of 0.45) [55]. The probe was modeled as initially starting in the center of the brain, implanted to a depth of 1.65 mm. In addition, mechanical strain was applied similarly by fixing the bottom surface of the brain cube and applying a 1 μm displacement in the thickness and width directions to model micromotion [55]. This simulation was used to determine the impact of the implanted electrode on tissue strain (Fig. 1ab).

Due to large differences in modulus between the brain tissue and the probe, ANSYS could not accurately determine the strain on the probe when simultaneously calculating the strain on the brain tissue. Therefore, the mechanical strain on the probe was modeled without the brain phantom; instead the strain was applied directly to the tip of the electrode (Fig. 1c–e). Previous models, as well as the above brain-electrode model showed that the greatest strain in the tissue occurs at the tip of the probe (Fig. 1b). This was modeled by fixing the electrode base and applying the same tip displacement as in the previous model, assuming forces between probe and tissue balance (Newton's third law).

3.2. Surgical Implantation

Single shank Michigan electrodes were implanted unilaterally into the left primary monocular visual cortex (V1m), of 9 wk old C57B6-Casp1 Knockout (n=3) and age matched C57B6 wildtype (n=3) female mice (22–28 g) [59]. The knockout of animals were used for studying the molecular and cellular pathways that mediate neural tissue response to

implants and the results are reported in our companion study [29]. While half of the examined electrodes were explanted from KO mice, implants in KO and WT animals are considered equivalent and mechanical failure modes of the electrode is not expected to be different across animal types. Each animal was anesthetized under 1.5% isoflurane and mounted onto a stereotaxic frame (Kopf Instruments, Tujunga, CA). The top surface of the skull was exposed and a drill sized craniotomy was made centered at 1 mm anterior to Lambda and 1.5 mm lateral to midline using a high speed dental drill and a .007 drill bit. Saline was applied continuously onto the skull to dissipate heat from the high-speed drill. Extra care was taken to prevent damage to the dura by reducing the drill speed and gently manually feeling the resistance of the skull when the dural blood vessels become visible through the opaque thin skull. A total of three bone screws were installed bilaterally over the primary motor cortex as well as over the contralateral visual cortex. The reference wire was connected to the bone screw over the contralateral visual cortex, while the ground wire was connected to both bone screws over the motor cortex. Arrays were inserted at ~2mm/s using a stereotaxic manipulator until the top edge of the last recording site was at the edge of the brain surface. Insertion of the array was visualized by a tilted surgical scope. The silicon device and the craniotomy were sealed carefully with silicone (Kwik-sil) and a headcap was created using UV-cured dental cement (Pentron Clinical, Orange CA). Animal temperature was maintained throughout the procedure using a warm water pad (HTP 1500, Adroit Medical Systems, Loudon TN). 0.3mg/kg buprenorphine was administered twice daily for three days as a post-operative analgesic. All animal care and procedures were performed under the approval of the University of Pittsburgh Institutional Animal Care and Use Committee and in accordance with regulations specified by the division of laboratory animal resources.

3.3. Neurophysiological Recording

Neural electrophysiology was recorded as previously described [27, 29]. Briefly, electrophysiological recordings were taken from the animal inside of a faraday cage with a visual stimulus-presenting computer monitor located outside of the cage. During each recording session, animals were situated on a microwaveable heating pad (Deltaphase isothermal pad, Braintree Scientific, Inc, Braintree, MA) inside of a darkened faraday cage (1.6 mm mesh) while lightly anesthetized with isoflurane. The faraday cage mesh size blocked major environmental noise (e.g. 60 Hz) without substantially blocking light from the monitor, which was placed just outside of the cage. The cage was grounded, but otherwise electrically isolated. Electrophysiological data was transferred outside of the cage through a nonconductive optic fiber via a battery-powered preamplifier (Medusa preamp, Tucker-Davis Technologies, Alachua FL) housed inside of the faraday cage using previously published methods [27]. Inputs and outputs from the cage were limited to gas or optical [27].

Visual stimuli were presented using the MATLAB-based Psychophysics toolbox [60–62] on a 24” LCD (V243H, Acer. Xizhi, New Taipei City, Taiwan) monitor placed 20 cm from the eye contralateral to the implant, spanning a visual field of 120° wide by 60° high. Drifting so lid black and white bar gratings were presented drifting in a perpendicular direction and synchronized with the recording system (RX7, Tucker-Davis Technologies, Alachua FL) at

24,414 Hz. Each 1 second of grating presentation (rotated in 45° increments) was separated by a 1 second dark screen period and the entire set was repeated 8 times per recording. Using Psychtoolbox, the timing of the visual stimulation was synchronized with the recording system (RX5, Tucker-Davis Technologies, Alachua FL) via transistor-transistor logic (TTL) pulses sent from the display computer through a stimulus isolator (A-M Systems Model 2200). The raw data stream was filtered from 0.3–5 kHz to produce spike data streams. Animal anesthesia level was set at the lowest concentration sufficient for the maintenance of animal inactivity (1.1% isoflurane in 1L/min O_2). Subjects were carefully observed during recording to ensure that the proper level of anesthesia was maintained. Proper level of anesthesia was defined as the lowest anesthesia concentration sufficient for maintaining animal inactivity while avoiding synchronous burst suppression neural activity which has been reported to produce poor evoked neural activity and synaptic transmission [63–65].

The spike data stream was further pre-processed using published methods [66, 67]. The raw data stream was filtered to produce the spike (300 – 5,000 Hz) data streams. The spike data stream was further pre-processed using the previously published common average referencing method [66]. To identify individual units, the threshold for the high-frequency data was established by using a window set at 3.5 standard deviations below the mean of the data [27, 66]. Offline spike sorting was carried out using a custom MATLAB script modified from previously published methods [27, 68]. A 1.2ms wave form snippet was extracted from the spike data stream upon threshold crossing. To isolate single neuronal units, the first 6 principal components (PCs) were calculated from the waveforms. The resultant components were used to separate the waveforms into individual clusters by a previously published automatic spike sorting method [69, 70] in the Chronux toolbox. Average single-unit signal-to-noise amplitude ratio was used to quantify electrode recording performance:

$$Single\ Unit SNAR = \mu_{SU-pp} \Big/ 2\sigma_N \quad [2]$$

where $\mu_{SU\text{-}pp}$ is the mean peak-to-peak amplitude of the waveform snippets and σ_N is the standard deviation of the spike data stream *after* all waveform snippets have been removed. If no single unit was detected, the signal-to-noise amplitude ratio (SNAR) was considered to be 0, unless otherwise stated, for the purposes of calculating average signal amplitude and SNAR. Only channels exhibiting sortable single unit spikes with SNAR >2 were analyzed. Candidate units with SNAR between 2 and 3 were manually confirmed or excluded by examining the combination of waveform shape, auto-correlogram, peak threshold crossing offset, and peri-stimulus time histogram (PSTH) with 50 ms bins. Candidate units with SNR below 2 were discarded, and candidate units with SNAR greater than 3 were manually confirmed by examining the waveform shape.

Using a photo-diode connected to a separate TDT analog input, the hardware & software delay for Psychophysics toolbox was measured, and the TTL trigger was realigned to the precise onset of the image drift on the computer screen. The threshold crossing multiunit PSTH of the visual stimulation trigger is calculated for each channel. Multi-unit (MU)

Signal-to-Noise Firing Rate Ratio (SNFRR) was defined as the average firing rate in a 550 ms bin of the 'ON' state minus the average firing rate of the 'OFF' state in a 550 ms bin after a 50 ms latency delay following the trigger divided by the average standard deviation of both the 'ON' and 'OFF' state.

$$SNFRR_{ON:OFF} = \frac{\mu_{on} - \mu_{off}}{\frac{1}{2}(\sigma_{on} - \sigma_{off})} \quad [3]$$

Two-sided Welch's T-test with the assumption of unequal variance ($p<0.05$) was conducted between 'ON' and 'OFF' firing rates. If no significant multi-unit was detected, MU amplitude and SNFRR were considered to be 0. A conservative Bonferroni correction was used to account for multiple comparisons ($p<0.05$, $\alpha<1.20\times10^{-4}$ (133 days) to $\alpha<9.83\times10^{-5}$ (189 days) depending on the # of time points). When the screen was occluded with cardboard, the visual stimulation did not induce any LFP, MU, or SU evoked response.

Current source density (CSD) to the evoked visual stimulus was used to identify Layer IV and used to align the recording depths across animals [71, 72]. Briefly, CSD was performed by computing the average evoked (stimulus-locked) LFP at each site, smoothing these signals across sites, and then calculating the second spatial derivative [71, 73]. We averaged the CSDs across 64 stimulus trials and determined the minimum value of the CSD in the first 100 ms. Polarity inversion of LFP was also examined to supplement the CSD analysis [74]. Layer IV was examined to study the changes of electrode depth over time and to align recording data across animals to a common Layer IV depth.

3.4. Impedance Spectroscopy

Electrochemical impedance was measured immediately after each neural recording session. While under anesthesia, the implanted array was connected to an Autolab potentiostat using a 16 channel multiplexer. Impedance was measured for each channel using a 10 mV RMS sine wave from 10 Hz to 32 kHz, employing a 15 multi-sine paradigm to shorten the time required for measurement. In this work, the 1 kHz impedance is reported unless indicated otherwise.

3.5. Immunohistochemistry

Animals were sacrificed and perfused according to University of Pittsburgh IACUC approved methods. Each animal was deeply anesthetized using a 90 mg/kg ketamine, 9 mg/kg xylazine cocktail. Once the proper plane of anesthesia was observed, animals were transcardially perfused using a warm PBS flush followed by ice cold 4% paraformaldehyde. Animals were decapitated, and heads were post-fixed in a 4% paraformaldehyde bath at 4°C for 4–6 hrs. Skulls containing the brain were t hen removed and soaked in a 15% sucrose bath at 4°C overnight followed by a 30% sucrose bath for 36–48 hours. Following sucrose protection, the bottom and sides of the skull was dissected and the brain was gently removed from the electrode array and headcap.

Arrays were rehydrated with 5 min washes with 1× phosphate buffer saline (PBS), repeated twice. Electrodes were gently broken off of the headcap at the base using forceps and placed

onto copper tape. The tissue sections were incubated in a blocking solution (5% goat serum, 0.1% triton X-100) for 0.5 hour at room temperature. Next, the tissue samples were blocked with AffiniPure Fab Fragment (Alexa-647 115-607-003 Jackson ImmunoResearch Laboratories, Inc.) for 2 hr then rinsed 8×4 min with 1× PBS.

Following blocking, sections were incubated in a primary antibody solution consisting of 5% goat serum, 0.1% triton X-100, and antibodies against Fibroblasts (1:250 Vimentin Clone V-9 Millipore) and microglia (1:250 Iba-1 NC9288364 Fisher) for 6 hours at room temperature in a humidifying chamber. Primary antibody solution was added every 2 hours to prevent the sample from drying out. Sections were then washed with PBS (3×5 min) and incubated in a secondary solution consisting of 5% goat serum, 1.5% triton X-100, and antibodies (1:500 goat anti-mouse Alexa 488, Invitrogen, and 1:500 goat anti-rabbit Alexa 568, Invitrogen, Carlsbad CA) for two hours at room temperature. Sections were then rinsed with PBS three times for 5 minutes each, and exposed to 1:1000 Hoechst 33342 (Invitrogen) for 10 minutes, and washed in PBS (3×5 min). Sections were stored in a humidifying chamber at 4C and promptly imaged within 8 hours using confocal microscopy (FluoView 1000, Olympus, Inc., Tokyo, Japan) at 20× magnification.

3.6. Scanning Electron Microscopy

Samples mounted on copper tape were coated with 3nm of Gold/Palladium (60/40) using a Cressington 108auto sputter coater (Watford, UK). Imaging was conducted on a JSM 6330F SEM (JEOL, Japan) at an accelerating voltage of 3kV. Working distance was adjusted automatically to allow for optimal image quality.

3.7. Magnetic Resonance Imaging

Human T1-weighted anatomical data were collected on a 3T GE MR750 system with a 32 channel receive coil (Nova Medical) using a magnetization prepared 3D fast spoiled gradient (FSPGR) sequence (TI=450ms, TE=3.18ms, 12° flip angle, 1mm slice thickness, FOV=25cm, 256×256×172 matrix size).

Cebus T1-weighted anatomical data were collected on a 3T Siemens Allegra system with a single channel receive coil (Nova Medical) using a 3D magnetization-prepared rapid gradient-echo (MPRAGE) sequence (TI=800ms, TE=3.04ms, TR=1580ms, 8° flip angle, 0.5mm slice thickness, FOV=12.8cm, 256×256×160 matrix size). The animal was anesthetized and its head was secured in a stereotaxic frame with ear bars to minimize head motion during scanning.

Mouse MRI images were acquired using a 9.4 Tesla magnet (Magnex, UK) with a 31 cm diameter bore equipped with a Unity INOVA console (Varian, CA) and a high-performance gradient coil. The animals were secured in a head-holder with ear and bite bars that suppress motion artifacts. A 1.2 cm diameter surface coil was placed on top of the mouse's head for imaging. A conventional gradient-echo acquisition was used to acquire anatomical images from 10 slices oriented axially across the brain (0.5 mm thick, 128 × 128 matrix, 2 × 2 cm^2 FOV, 4 ms TE, 100 ms TR, 90 degree FA).

4. Results

The FEM of the silicon electrode contained 2,469,029 nodes and 1,575,175 elements. Since the critical dimension (thickness) is the least in the direction normal to the planar surface of the probe, it is expected that mechanical failure is most likely to occur in this dimension. Therefore, the computational analysis was focused on the displacement in the direction normal to the surface of the probe.

As shown in previous studies [54, 55], we confirm the observation that when a small 1 μm displacement is applied to an implanted silicon electrode, the strain in the tissue is greatest at the tip of the electrode (Fig. 1a). Because of the large differences in elastic modulus between the probe and the brain tissue, the small mesh sizes required to accurately model the electrical trace structures, and limited capabilities of the software, it was necessary to model the electrode strain without the brain tissue model. Therefore, we applied the focal point of the displacement on the tip corner of the electrode while fixing the back of the electrode, as it would be when dental cemented to the skull (Fig. 1e).

4.1. Structural Analysis via Finite Element Modeling

The von Mises Equivalent Elastic Strain FEM shows that there is elevated strain around the edges of the Iridium electrode sites (Fig. 2a). Further, the edges of the protruding electrode traces show the greatest level of strain around the electrode. Examining the cross-section of the model shows that the strain is substantially lower inside the substrate than along the surfaces (Fig. 3a, Fig. S6). To further quantify these differences, the strain level on top of the trace, the surface of the substrate next to the trace, and the interior of the substrate away from the 5^{th} and 6^{th} recording sites were plotted (Fig. 3a–c), which reaffirms that the strain is the greatest at the surface of the protruded electrical trace structures, especially near the electrode recording sites.

4.2. SEM Analysis of Structural Failure in Planar Electrodes

Chronically implanted electrodes (133 to 189 days) were explanted and examined using scanning electron microscopy. The SEM images showed that electrical traces had cracked and degraded around the recording sites (Fig. 2b, 3d, Fig. S5, S7). The structural degradation patterns coincided with the regions showing the greatest strain in the model. Interestingly, the structural integrity of the traces appeared to be intact in the regions between the electrode sites where the strain level was much lower (Fig. 2b, 3d, Fig. S5, S7).

4.3. Chronic Recording and Impedance Data

To determine that the mechanical failure mode predicted with FEM and observed under the SEM occurred *in vivo* as opposed to during the implantation, removal, staining, and mounting process, the *in vivo* electrophysiology and impedance spectra data were examined (Fig. 4–8). SU SNAR and evoked MU $SNFFR_{ON:OFF}$ decreases accompanied either large increases (>>2MΩ) or large decreases in impedance (>200kΩ from starting value) (Fig. 4–7). Figure 4a shows an electrode with substantial material degradation of the electrical traces (more images can be found in Fig. S5). Impedance (Fig 4d) and noise floor (Fig 4e) sharply increased on day 175, which was accompanied by loss of all single-unit and multi-unit

recordings (Fig 4bc). The bode plots (Fig 4fg) for both magnitude and phase showed dramatic changes at day 175, while Nyquist plot (fig 4h) suddenly exhibited a large RC arc and lower tail slope. The large RC arc appearance has been associated with 'extensive' tissue reaction in a different study [75]. However, immunohistochemistry staining of the probe shows limited cellular adhesion (Fig. 4i) while the SEM reveals extensive degradation of electrical traces, suggesting the drastic change in Nyquist behavior is associated with electrical failure. The RC arc may be from changes in the silicon oxide insulation or the capacitive charge transfer mode of the exposed polysilicon trace instead of cellular encapsulation. Lastly, Figure 4i shows scattered cellular debris and membrane over the substrate where the traces used to lie before degradation, further supporting that the mechanical failure occurred in vivo (see also Fig. S5 for additional magnification).

Similarly, Figure 5a shows an SEM image with cracked and degraded traces around a recording electrode in which SU and MU recordings disappeared after 42 days (Fig 5bc). 1 kHz impedance (Fig 5d) showed a sharp increase (>2MΩ) on day 35 suggesting trace failure, which resulted in the electrode disconnect. This sharp increase was also observed in the noise floor (Fig 5e).Scattered or jagged (noisy) curves in the Bode Phase and Nquist plot on day 35 indicate a break in the electrical circuit. After 42 days, the 1 kHz impedance sharply dropped, and noise floor steadily declined. SEM data shows cracks over the electrical traces suggesting the decrease in impedance is due to breakdown of the silicon oxide insulation. The subsequent smooth Bode and Nyquist plots further support the de-insulation and increased surface area of the exposed electrical trace. These two situations, represented in Figures 4 and 5, indicate that material failure of the electrode can exhibit either an increase in impedance or a decrease in impedance.

4.4. Complex In Vivo Failure and Partial Recovery

Intact electrical traces next to the recording sites do not necessarily guarantee the health of the electrode, the traces could also be damaged as they pass by other recording sites higher on the electrode (Fig. 6). Figure 6a shows an SEM image of a recording site with an intact electrical trace adjacent to the electrode. However, the 1 kHz impedance and noise floor dramatically dropped between 14 and 28 days post-implant (Fig. 6de). Bode Magnitude also showed a substantial drop at this time (Fig. 6f), and the Bode phase generally shifted down in lower frequencies (Fig. 6g). Closer examination of the array showed that material degradation of electrical trace for this channel (channel #1) occurred as it passes another recording site (channel #3) (Fig 6i). Breakdown of the insulation can increase the interfacial surface area, decreasing impedance. Interestingly, starting around 154 days, some recording performance and impedance recovered to initial values. The Bode Magnitude and Bode Phase returned to early time point values at higher frequencies, although they remain low for lower frequencies. While substantial shifts in the Nyquist can be observed, signs of the complex RC spectra were limited, and the resistance increased from days 147 to 175 (Fig. 6h). These data suggest that after the insulation breakdown, the electrical trace failed disconnecting the Ir recording site and decreasing the exposed surface area of the electrical trace. Remarkably, evoked multi-unit activity generally remains detectable throughout the implant period. It is possible that this reduced surface area make it possible to detect low quality spike signals.

Cellular encapsulation can also affect recording performance (Fig. 7). Figure 7 shows a recording site that was encapsulated by glial cells that are Iba-1, IgG, and vimentin positive (Fig 7a,i). Impedance and noise were seen increasing over the first week and then dramatically declined over the next two weeks (Fig. 7de). The increase in impedance could be from cellular encapsulation or electrical trace failure, while the dramatic drop in impedance was most likely from insulation failure. The loss of single-unit recording coincided with the drop in impedance and noise (Fig. 7b–e). Over the next four weeks, both impedance and noise steadily increased and the tail slope of the nyquist plot decreased. SEM and immunohistochemistry suggest that this was due to glial encapsulation of the electrode (Fig. 7a,i). Interestingly, at very chronic time points, single-units were periodically detected. It may be possible that the glial encapsulation reduced the surface area that had initially increased from de-insulation leading to the low quality spike recording at very chronic time points. The combination of impedance drop, material deinsulation, and glial encapsulation can cause complex electrode performance behavior.

4.5. Variability and Unpredictability of Mechanical Failure Mode

While chronic *in vivo* validation of the FEM was demonstrated, failure was not observed in all recording sites. Recording sites in Figure 8 showed intact electrical traces (see also Fig. S8). This recording site was accompanied by more stable impedances over time as well as good SU and MU chronic recordings. The 1 kHz, noise floor, and Bode Magnitude spectra remain stable after a slight increase in first week, most likely due to insertion injury repair and tissue integration. While some longitudinal shifts could be observed in the Bode Phase and change in the charge transfer resistance component of the Nyquist, the Nyquist tail slope in the lower frequencies remain largely stable. It should be noted, however, that the traces around the edge of the Ir electrode show small perforations in the insulation, which may develop into performance failure at longer time.

4.6. MRI Provides Insight into Electrode Failure Discrepancy Between Animal Models

Images of the head were obtained using MRI from different animal species with sufficient contrast to distinguish the distance between the cortex and overlaying layers of skull, muscle and skin (Fig. 9a–c). It is evident that the interstitial distance from skin/skull to cortex diminishes with head size, from about 2~4 mm in humans (Fig. 9d) and ~1 mm monkeys (Fig. 9e) to ~0.1–0.2 mm in rodents (Fig. 9f). Therefore, an electrode that experiences 0.1 mm displacement in normal brain movement in rodents will experience greater displacement (1–4 mm) from a proportional movement in primates. This would result in greater mechanical strain on the same electrode in primates when compared to rodents.

5. Discussion

5.1. Architecture and Mechanical Mismatch within an Electrode

While mechanical mismatch and mechanical strain between the brain and electrode have been described [12, 29, 54, 55, 76], the mechanical mismatch between different materials and different structural components within a device have not been comprehensively characterized. The results presented here demonstrate that mechanical mismatch between iridium metal and silicon substrates leads to strain concentration along the border of the two

materials. This strain is further focused on small protrusions such as the electrical lead traces in planar silicon electrodes. To simplify the model, the silicon oxide, and polysilicon traces were modeled with the same properties of the bulk silicon. Silicon oxide, and polysilicon are known to be more brittle than bulk silicon with lower fracture strength. Therefore, the model should be considered as a conservative estimation.

In addition, Von Mises Equivalent Strain along the device cross-section shows that the protruding trace experiences the greatest strain because when the device is deformed, the surfaces experience the largest compression or elongation while the center experiences the least. Therefore, embedding the electrical leads deep in the substrate may improve the structural integrity of the electrical traces, though this adds a greater level of complexity to microfabrication. In addition, failure of the various array components is influenced by both the strains generated by geometry and physical properties of the materials. Not only does the architecture increase the strain focused on the insulting silicon oxide, it has the lowest fracture strength when compared to bulk silicon, polysilicon, and iridium. Furthermore, due to the continuous tapering nature of the silicon Michigan electrodes, the traces near the tip recording sites experience the greatest level of strain. While this FEM study did not model fatigue or failure, Von Mises Equivalent Strain highlighted which regions of the electrode were most vulnerable.

In vivo studies confirmed the failure modes (Fig. 4–7). Cracking and delaminations of traces in vivo have been frequently observed with more incidences occurring at the vicinity of the electrode sites where the strain is most concentrated. Sharp increase in impedance (>2MΩ) can indicate trace failure, due to breakage of the electrical connection to the electrode (Fig. 4). When electrode trace degrades and completely breaks down, the impedance Bode plot can show a large increase in modulus and Nyquist plot shows scattered data points (non-continuous curve) due to the inability of the potentiostat to accurately detect the very small and noisy open circuit currents. These features can be used to easily identify electrical connection failure of the electrode.

However, examining the Nyquist and Bode spectra data alone cannot always identify electrode failure from trace de-insulation (Fig. 5). A sharp or continuous decrease in impedance suggests progression of trace deinsulation as the brittle insulating silicon oxide cracks and fails. The combined exposed surface area of the recording site and un-insulated electrode trace increases the electrode-electrolyte surface area. This can cause the impedance modulus to fall below the initial values or *in vitro* pre-implant values (609 ± 19 kΩ). These examples suggest that a dramatic decrease in impedance can also signal mechanical electrode failure. This is more difficult to identify due to the fact that impedance decreases from insulation failure still show smooth Bode Magnitude and Nyquist plots.

Furthermore, the insulation around an electrode may be intact (Fig. 6), but the electrical trace can break as it passes next to a different recording site further up the shank. This would increase the probability that deeper recording sites will be more likely to fail compared to recording sites closer to the base of the array. It is also possible that the trace can be completely disconnected from the recording site and yet also be de-insulated in a shallower region. Our data suggests that it may be possible for de-insulated traces (indicated by a

chronic drop in impedance below starting values) to detect low amplitude SU or MU activity. Alternatively, a partial glial sheath may 'insulate' an exposed (deinsulated) electrical trace, reducing the recording site surface area to one consistent with detecting SU and MU activity (Fig. 7). It should be noted that not all recording sites failed, adding to the complexity of variability and unpredictability (Fig. 8). Good SU and MU activity were recorded on many of these recording sites. Regardless of the electrode type used, insulation failure remains a common form of material electrode failure [39, 40, 77].

5.2. Comparison to Polymer Material Failure Mode

Mechanical strain in the tissue surrounding intracortical electrodes has been observed *in vivo* and has been shown to aggravate the host tissue response to the implant [12, 76]. Increased tissue strain has been shown to upregulate many proinflammatory cytokines including Interleukin-1β (IL-1β), which is activated by caspase-1 [29, 76]. Knocking out caspase-1 significantly ($p<0.05$) improved single-unit recording performance, demonstrating the influence of mechanical strain on cellular functionality and electrode performance *in vivo* [29].

These past and emerging studies have motivated the development of compliant or flexible implantable intracortical electrode arrays using polymer substrates such as parylene, polyimide, and polydimethylsiloxane (PDMS) [78–89]. Despite the promise of decreasing the tissue strain local to the implant, compliant polymer electrodes face numerous challenges in practical implementation for chronic intracortical neural recording. These materials showed poor dimensional stability [90]. Cracking of thin-film conductors (such as Pt and Au) during fabrication, assembly, and insertion have been reported [90], as well as water absorption which causes expansion, leakage, and extra mechanical strain on the tissue [91]. In addition, planar polymer devices are typically fabricated by sandwiching thin-film metal traces with two layers of polymers. When two layers of crystalline polymers are deposited in series, a grain boundary forms between the two polymer layers. Once these devices are implanted, two adjoining crystalline polymer layers and the surrounding aqueous environment of the tissue form a triple junction (Fig. S9) [92–98]. The irreversible thermodynamics of crack propagation and cavitation at a triple-junction have been well characterized, especially in highly ionic liquids such as the cerebral spinal fluid [99–106], and is observed as a significant drop in impedance [107, 108] shortly after exposure to saline.

While thermal annealing processes have decreased delamination, they have been shown to negatively impact sensitivity [107]. Research and exploration of amorphous (non-crystalline) polymers may be one approach to forming more permanent thermally annealed insulators. Another alternative is to conformally and seamlessly insulate substrates and traces that are floating or suspended (with appropriate sacrificial masks) [89]. In contrast, simple designs such as microwires and bed of needle arrays that are conformally coated with a single layer of polymer insulation may bypasses this polymer-polymer delamination failure. Nevertheless, these devices also suffer from conductor-polymer delamination and insulation cracks near the recording tip [20, 39, 40].

Another approach is the use of temperature and water-sensitive polymers that are stiff prior to insertion, but become softer after implantation [88, 90]. These materials present challenges in the fabrication of functional devices due to poor dimensional stability during microfabrication [90]. These planar polymer devices generally have improved structural designs than their planar silicon device counter-part by burying the electrical traces in the center of the device. However, the polymer substrate, thin-film metal traces, and electrode recording sites have a greater discrepancy in the mechanical mismatch within the probe. As a result, cracking of thin-film conductors during fabrication, assembly, and insertion have been reported as a technical challenge [90].

5.3. Variability from Wafer non-uniformity

Our results showed large variability in the number of electrode sites across arrays that experience mechanical failure (3/16 to >10/16) as well as time points of failure. Device variability can occur during microfabrication. Subtle differences in the environmental conditions, such as local temperature distribution, or reagents can impact fabrication yield and quality between different fabrication runs or lots, even within a highly controlled state-of-the-art clean room. Other studies have shown large variability can occur within a single wafer. The distribution of reactants becomes thinner at the edges of the wafer [109]. As a result, devices near the center of the wafer generally have higher yield and quality. This information is generally not tracked by the manufacturer, so it was not possible to draw any correlations. Variability during microfabrication may be one contributor of longitudinal recording performance variability.

5.4. Effects of Brain and Skull Size on Mechanical Displacement, Strain, and Mechanical Failure

While planar electrodes are ideal for certain neuroscience research, such as understanding the laminar organization along a cortical column, traditional 15 μm thick silicon devices are considered to be too fragile for chronic studies in primates [53]. On the other hand, these same devices are used abundantly in rats and mice chronic studies with varying degrees of success depending on the duration of the study [110–113]. The reactive tissue responses to implants have been reported to be similar between rodents and non-human primates [114, 115]. To determine a possible reason for this discrepancy, the amount of interstitial space between the brain and skull in humans (2~4 mm), and monkeys (~1 mm) were compared to mice (0.1~0.2 mm) (Fig. 9d–f). Larger space will allow higher displacement of the probe resulting in higher strain. Furthermore, the significantly larger size of primates brains (adult humans 1,300~1,400 g,cebus monkeys 60~80 g, rhesus monkeys 90~97 g, Rats ~2g, and mice 0.3–0.5 g) and the greater maximum force the animal can generate also lead to much greater mechanical strain compared to rodents [116–121].

5.5. Future Directions

Recent studies have motivated the development of ultra-small microelectrodes [17, 27, 28, 33, 83, 122–124]. The reduction of the feature size automatically increases the flexibility of the device [27]. Furthermore, ultra-small microelectrodes with sub-cellular feature sizes have shown reduced reactive tissue response [27, 28, 122, 123]. More importantly, these sub-cellular featured microelectrodes have been shown to improve longitudinal recording

performance [27, 124]. However, reducing feature size focuses the mechanical strain over a smaller area of the probe and thereby decreases the structural integrity of implantable electrodes. Composite conductors are an approach being actively explored as flexible alternatives to the brittle thin-film metal traces [32, 33, 125–130]. Small, yet strong carbon fiber based Microthread electrodes show more evenly distributed strain due to the lack of sharp edges and corners (Fig. 10). In addition, Layer-by-Layer assembly of polyelectrolytes in particular have demonstrated great potential in forming self-healing material [131]. Since the individual particles in the layers are non-covalently bonded, they are highly mobile resulting in the materials flexibility and ability to heal defects. 'Smart' self-healing polymers are also being explored for the insulating dielectric material [132]. Some polymers have the ability to be functionalized with reactive chemical species [27, 133–144], which can be used to provide the device with self-healing properties. For example, planar parylene array designs where the two parylene layers were deposited with complementary reactive functional groups [108]. The reactive functional groups form an imine bond that chemically seals the two parylene layers. This study showed even when the two layers were not thermally annealed, self-annealing can occur *in vitro* over time. As the bonds between the layers are broken or the material degrades, the existing functional groups or newly exposed functional groups may reseal the crack between the two insulation layers through an exothermic reaction. However, additional research is still necessary to understand the dynamics of this self-healing property *in vivo*. These emerging materials and design should be considered when addressing chronic mechanical failure modes.

6. Conclusion

This study showed for the first time that the mechanical strain within a planar microelectrode array caused by motion is focused around electrode sites and on the protruded electrical traces. Longitudinal *in vivo* experiments validated electrode failure during the implant period in the regions predicted by the FEM. This study highlights the importance of considering the microarchitecture and mechanical mismatch between substructures and various material components during electrode design, as well as the importance of considering the difference in magnitude of physiological motion and macromotion experienced by the electrode when scaling up to larger animal models.

Supplementary Material

Refer to Web version on PubMed Central for supplementary material.

Acknowledgement

The authors would like to thank Jeyakumar Subbaroyan and John Seymour for valuable discussion with FEM and NeuroNexus Electrodes, Cynthia A. Chestek for helpful discussions with primates, and Zhanhong 'Jeff' Du for assistance with chronic recordings. The authors would also like to thank Lance M. Bodily and Ellen M. Caparosa for assistance with surgery, Machiko Obayashi and Peter L. Strick for the use of a Cebus monkey anatomical (with support provided by NIH P30 NS076405 and R01 NS24328), and Hunter Meherns for the mouse anatomical data. Confocal microscopy and SEM were conducted at the University of Pittsburgh Center for Biological Imaging. This work was financially supported by an NIH R01 (5R01NS062019) and The Pittsburgh Foundation.

References

1. Smith MA, Jia X, Zandvakili A, Kohn A. Laminar dependence of neuronal correlations in visual cortex. J Neurophysiol. 2013; 109:940–947. [PubMed: 23197461]
2. Lee JH, Whittington MA, Kopell NJ. Top-down beta rhythms support selective attention via interlaminar interaction: a model. PLoS Comput Biol. 2013; 9:e1003164. [PubMed: 23950699]
3. Hampson RE, Gerhardt GA, Marmarelis V, Song D, Opris I, Santos L, et al. Facilitation and restoration of cognitive function in primate prefrontal cortex by a neuroprosthesis that utilizes minicolumn-specific neural firing. J Neural Eng. 2012; 9:056012. [PubMed: 22976769]
4. Anderson LA, Christianson GB, Linden JF. Mouse auditory cortex differs from visual and somatosensory cortices in the laminar distribution of cytochrome oxidase and acetylcholinesterase. Brain Research. 2009; 1252:130–142. [PubMed: 19061871]
5. Sales-Carbonell C, Rueda-Orozco PE, Soria-Gomez E, Buzsaki G, Marsicano G, Robbe D. Striatal GABAergic and cortical glutamatergic neurons mediate contrasting effects of cannabinoids on cortical network synchrony. Proc Natl Acad Sci U S A. 2013; 110:719–724. [PubMed: 23269835]
6. Patel J, Fujisawa S, Berenyi A, Royer S, Buzsaki G. Traveling theta waves along the entire septotemporal axis of the hippocampus. Neuron. 2012; 75:410–417. [PubMed: 22884325]
7. Royer S, Zemelman BV, Losonczy A, Kim J, Chance F, Magee JC, et al. Control of timing, rate and bursts of hippocampal place cells by dendritic and somatic inhibition. Nat Neurosci. 2012; 15:769–775. [PubMed: 22446878]
8. Mizuseki K, Royer S, Diba K, Buzsaki G. Activity dynamics and behavioral correlates of CA3 and CA1 hippocampal pyramidal neurons. Hippocampus. 2012; 22:1659–1680. [PubMed: 22367959]
9. Belluscio MA, Mizuseki K, Schmidt R, Kempter R, Buzsaki G. Cross-frequency phase-phase coupling between theta and gamma oscillations in the hippocampus. The Journal of neuroscience : the official journal of the Society for Neuroscience. 2012; 32:423–435. [PubMed: 22238079]
10. Haider B, Hausser M, Carandini M. Inhibition dominates sensory responses in the awake cortex. Nature. 2013; 493:97–100. [PubMed: 23172139]
11. Gage GJ, Stoetzner CR, Wiltschko AB, Berke JD. Selective activation of striatal fast-spiking interneurons during choice execution. Neuron. 2010; 67:466–479. [PubMed: 20696383]
12. Kozai TDY, Vazquez AL, Weaver CL, Kim SG, Cui XT. In vivo two photon microscopy reveals immediate microglial reaction to implantation of microelectrode through extension of processes. J Neural Eng. 2012; 9:066001. [PubMed: 23075490]
13. Collinger JL, Wodlinger B, Downey JE, Wang W, Tyler-Kabara EC, Weber DJ, et al. High-performance neuroprosthetic control by an individual with tetraplegia. Lancet. 2012; 381(9866): 557–564. [PubMed: 23253623]
14. Hochberg LR, Bacher D, Jarosiewicz B, Masse NY, Simeral JD, Vogel J, et al. Reach and grasp by people with tetraplegia using a neurally controlled robotic arm. Nature. 2012; 485:372–375. [PubMed: 22596161]
15. Gilja V, Nuyujukian P, Chestek CA, Cunningham JP, Yu BM, Fan JM, et al. A high-performance neural prosthesis enabled by control algorithm design. Nature neuroscience. 2012; 15:1752–1757.
16. Freire MA, Morya E, Faber J, Santos JR, Guimaraes JS, Lemos NA, et al. Comprehensive analysis of tissue preservation and recording quality from chronic multielectrode implants. PLoS One. 2011; 6:e27554. [PubMed: 22096594]
17. Kozai TDY, Marzullo TC, Hooi F, Langhals NB, Majewska AK, Brown EB, et al. Reduction of neurovascular damage resulting from microelectrode insertion into the cerebral cortex using in vivo two-photon mapping. J Neural Eng. 2010; 7:046011. [PubMed: 20644246]
18. Williams JC, Rennaker RL, Kipke DR. Long-term neural recording characteristics of wire microelectrode arrays implanted in cerebral cortex. Brain Res Brain Res Protoc. 1999; 4:303–313. [PubMed: 10592339]
19. Rousche PJ, Normann RA. Chronic recording capability of the Utah Intracortical Electrode Array in cat sensory cortex. J Neurosci Methods. 1998; 82:1–15. [PubMed: 10223510]
20. Prasad A, Xue QS, Dieme R, Sankar V, Mayrand RC, Nishida T, et al. Abiotic-biotic characterization of Pt/Ir microelectrode arrays in chronic implants. Front Neuroeng. 2014; 7:2. [PubMed: 24550823]

21. Johnson MD, Kao OE, Kipke DR. Spatiotemporal pH dynamics following insertion of neural microelectrode arrays. J Neurosci Methods. 2007; 160:276–287. [PubMed: 17084461]
22. Barrese JC, Rao N, Paroo K, Triebwasser C, Vargas-Irwin C, Franquemont L, et al. Failure mode analysis of silicon-based intracortical microelectrode arrays in non-human primates. Journal of Neural Engineering. 2013; 10:066014. [PubMed: 24216311]
23. Chestek CA, Gilja V, Nuyujukian P, Foster JD, Fan JM, Kaufman MT, et al. Long-term stability of neural prosthetic control signals from silicon cortical arrays in rhesus macaque motor cortex. Journal of Neural Engineering. 2011; 8:045005. [PubMed: 21775782]
24. Stensaas SS, Stensaas LJ. The reaction of the cerebral cortex to chronically implanted plastic needles. Acta Neuropathol. 1976; 35:187–203. [PubMed: 782142]
25. Woolley AJ, Desai HA, Otto KJ. Chronic intracortical microelectrode arrays induce non-uniform, depth-related tissue responses. Journal of Neural Engineering. 2013; 10:026007. [PubMed: 23428842]
26. Kozai TD, Marzullo TC, Hooi F, Langhals NB, Majewska AK, Brown EB, et al. Reduction of neurovascular damage resulting from microelectrode insertion into the cerebral cortex using in vivo two-photon mapping. J Neural Eng. 2010; 7:046011. [PubMed: 20644246]
27. Kozai TDY, Langhals NB, Patel PR, Deng X, Zhang H, Smith KL, et al. Ultrasmall implantable composite microelectrodes with bioactive surfaces for chronic neural interfaces. Nature materials. 2012; 11:1065–1073.
28. Kozai TDY, Gugel Z, Li X, Gilgunn PJ, Khilwani R, Ozdoganlar OB, et al. Chronic tissue response to carboxymethyl cellulose based dissolvable insertion needle for ultra-small neural probes. Biomaterials. 2014; 35:9255–9268. [PubMed: 25128375]
29. Kozai TDY, Li X, Bodily LM, Caparosa EM, Zenonos GA, Carlisle DL, et al. Effect of caspase-1 knockout on chronic neural recording quality and longevity: Insight into cellular and molecular mechanisms of the reactive tissue response. Biomaterials. 2014; 35:9620–9634. [PubMed: 25176060]
30. Barrese JC, Rao N, Paroo K, Triebwasser C, Vargas-Irwin C, Franquemont L, et al. Failure mode analysis of silicon-based intracortical microelectrode arrays in non-human primates. J Neural Eng. 2013; 10:066014. [PubMed: 24216311]
31. Saxena T, Karumbaiah L, Gaupp EA, Patkar R, Patil K, Betancur M, et al. The impact of chronic blood-brain barrier breach on intracortical electrode function. Biomaterials. 2013
32. Kozai TDY, Langhals NB, Patel PR, Deng X, Zhang H, Smith KL, et al. Supplementary Information: Ultrasmall implantable composite microelectrodes with bioactive surfaces for chronic neural interfaces. Nature materials. 2012; 11 Supplementary Information.
33. Kozai, T.; Alba, N.; Zhang, H.; Kotov, N.; Gaunt, R.; Cui, X. Nanostructured coatings for improved charge delivery to neurons. In: Vittorio, MD.; Martiradonna, L.; Assad, J., editors. Nanotechnology and neuroscience: nano-electronic, photonic and mechanical neuronal interfacing. New York, NY: Springer New York; 2014. p. 71-134.
34. Kozai, T.; Marzullo, T.; Hooi, F.; Langhals, N.; Majewska, A.; Brown, E., et al. Reduction of neurovascular damage resulting from microelectrode insertion into cerebral cortex using in vivo two-photon mapping. Society for Neuroscience; 39th Annual Meeting; Oct 17–21; Chicago, IL. 2009.
35. Bjornsson CS, Oh SJ, Al-Kofahi YA, Lim YJ, Smith KL, Turner JN, et al. Effects of insertion conditions on tissue strain and vascular damage during neuroprosthetic device insertion. J Neural Eng. 2006; 3:196–207. [PubMed: 16921203]
36. Saxena T, Karumbaiah L, Gaupp EA, Patkar R, Patil K, Betancur M, et al. The impact of chronic blood-brain barrier breach on intracortical electrode function. Biomaterials. 2013; 34:4703–4713. [PubMed: 23562053]
37. Nordhausen CT, Maynard EM, Normann RA. Single unit recording capabilities of a 100 microelectrode array. Brain Research. 1996; 726:129–140. [PubMed: 8836553]
38. Drake KL, Wise KD, Farraye J, Anderson DJ, BeMent SL. Performance of planar multisite microprobes in recording extracellular single-unit intracortical activity. IEEE Trans Biomed Eng. 1988; 35:719–732. [PubMed: 3169824]

39. Prasad A, Xue QS, Sankar V, Nishida T, Shaw G, Streit WJ, et al. Comprehensive characterization and failure modes of tungsten microwire arrays in chronic neural implants. J Neural Eng. 2012; 9:056015. [PubMed: 23010756]
40. Gilgunn, PJ.; Xiao Chuan, O.; Flesher, SN.; Schwartz, AB.; Gaunt, RA. Structural analysis of explanted microelectrode arrays. Neural Engineering (NER); 2013 6th International IEEE/EMBS Conference on; 2013. p. 719-722.
41. Gratiy SL, Devor A, Einevoll GT, Dale AM. On the estimation of population-specific synaptic currents from laminar multielectrode recordings. Front Neuroinform. 2011; 5:32. [PubMed: 22203801]
42. Blomquist P, Devor A, Indahl UG, Ulbert I, Einevoll GT, Dale AM. Estimation of thalamocortical and intracortical network models from joint thalamic single-electrode and cortical laminar-electrode recordings in the rat barrel system. PLoS Comput Biol. 2009; 5:e1000328. [PubMed: 19325875]
43. Einevoll GT, Pettersen KH, Devor A, Ulbert I, Halgren E, Dale AM. Laminar population analysis: estimating firing rates and evoked synaptic activity from multielectrode recordings in rat barrel cortex. J Neurophysiol. 2007; 97:2174–2190. [PubMed: 17182911]
44. Cheung, K.; Gun, L.; Djupsund, K.; Yang, D.; Lee, LP. A new neural probe using SOI wafers with topological interlocking mechanisms. Microtechnologies in Medicine and Biology; 1st Annual International, Conference On; 2000. p. 507-511.2000
45. Najafi K, Suzuki K. Measurement of fracture stress, Young's modulus, and intrinsic stress of heavily boron-doped silicon microstructures. Thin Solid Films. 1989; 181:251–258.
46. Sharpe WN Jr, Pulskamp J, Gianola DS, Eberl C, Polcawich RG, Thompson RJ. Strain Measurements of Silicon Dioxide Microspecimens by Digital Imaging Processing. Exp Mech. 2007; 47:649–658.
47. Sharpe, WN.; Yuan, B.; Vaidyanathan, R.; Edwards, RL. Measurements of Young's modulus, Poisson's ratio, and tensile strength of polysilicon. Micro Electro Mechanical Systems, 1997 MEMS '97; Proceedings, IEEE, Tenth Annual International Workshop on; 1997. p. 424-429.
48. Hunt LB. A History of Iridium. Platinum Metal Review. 1987; 31:32–41.
49. Berenyi A, Somogyvari Z, Nagy AJ, Roux L, Long JD, Fujisawa S, et al. Large-scale, high-density (up to 512 channels) recording of local circuits in behaving animals. Journal of Neurophysiology. 2014; 111:1132–1149. [PubMed: 24353300]
50. Mizuseki K, Buzsaki G. Preconfigured, skewed distribution of firing rates in the hippocampus and entorhinal cortex. Cell Rep. 2013; 4:1010–1021. [PubMed: 23994479]
51. Caixeta FV, Cornelio AM, Scheffer-Teixeira R, Ribeiro S, Tort AB. Ketamine alters oscillatory coupling in the hippocampus. Sci Rep-Uk. 2013; 3:2348.
52. von Pfostl V, Li J, Zaldivar D, Goense J, Zhang X, Serr N, et al. Effects of lactate on the early visual cortex of non-human primates, investigated by pharmaco-MRI and neurochemical analysis. Neuroimage. 2012; 61:98–105. [PubMed: 22426350]
53. Sakamoto, K.; Matsuzaka, Y.; Suenaga, T.; Watanabe, H.; Kobayashi, R.; Fukushima, T., et al. A simple device allowing silicon microelectrode insertion for chronic neural recording in primates. Neural Engineering; 2009 NER '09 4th International IEEE/EMBS Conference on; 2009. p. 104-107.
54. Lee H, Bellamkonda RV, Sun W, Levenston ME. Biomechanical analysis of silicon microelectrode-induced strain in the brain. J Neural Eng. 2005; 2:81–89. [PubMed: 16317231]
55. Subbaroyan J, Martin DC, Kipke DR. A finite-element model of the mechanical effects of implantable microelectrodes in the cerebral cortex. J Neural Eng. 2005; 2:103–113. [PubMed: 16317234]
56. Sridharan A, Rajan SD, Muthuswamy J. Long-term changes in the material properties of brain tissue at the implant-tissue interface. J Neural Eng. 2013; 10:066001. [PubMed: 24099854]
57. Lee, H-H. Finite Element Simulations with ANSYS Workbench 14. Mission, KS: Schroff Development Corporation; 2012.
58. Hugonist, S. Report LA-4167-MS, Group GMX-6. Los Alamos: Los Alamost Scientific Laboratory, University of California; 1969. NM-86544.

59. Friedlander RM, Gagliardini V, Hara H, Fink KB, Li W, MacDonald G, et al. Expression of a dominant negative mutant of interleukin-1 beta converting enzyme in transgenic mice prevents neuronal cell death induced by trophic factor withdrawal and ischemic brain injury. J Exp Med. 1997; 185:933–940. [PubMed: 9120399]
60. Brainard DH. The Psychophysics Toolbox. Spat Vis. 1997; 10:433–436. [PubMed: 9176952]
61. Pelli DG. The VideoToolbox software for visual psychophysics: transforming numbers into movies. Spat Vis. 1997; 10:437–442. [PubMed: 9176953]
62. Kleiner M, Brainard DH, Pelli DG. What's new in Psychtoolbox-3? Perception. 2007; 36 ECVP Abstract Supplement.
63. Goncalves JT, Anstey JE, Golshani P, Portera-Cailliau C. Circuit level defects in the developing neocortex of Fragile X mice. Nature neuroscience. 2013; 16:903–909.
64. Mukamel EA, Pirondini E, Babadi B, Wong KF, Pierce ET, Harrell PG, et al. A transition in brain state during propofol-induced unconsciousness. The Journal of neuroscience : the official journal of the Society for Neuroscience. 2014; 34:839–845. [PubMed: 24431442]
65. Hudson AE, Calderon DP, Pfaff DW, Proekt A. Recovery of consciousness is mediated by a network of discrete metastable activity states. Proceedings of the National Academy of Sciences. 2014
66. Ludwig KA, Miriani RM, Langhals NB, Joseph MD, Anderson DJ, Kipke DR. Using a common average reference to improve cortical neuron recordings from microelectrode arrays. J Neurophysiol. 2009; 101:1679–1689. [PubMed: 19109453]
67. Wagenaar DA, Potter SM. Real-time multi-channel stimulus artifact suppression by local curve fitting. Journal of Neuroscience Methods. 2002; 120:113–120. [PubMed: 12385761]
68. Fee MS, Mitra PP, Kleinfeld D. Automatic sorting of multiple unit neuronal signals in the presence of anisotropic and non-Gaussian variability. Journal of Neuroscience Methods. 1996; 69:175–188. [PubMed: 8946321]
69. Fee MS, Mitra PP, Kleinfeld D. Automatic sorting of multiple unit neuronal signals in the presence of anisotropic and non-Gaussian variability. Journal of Neuroscience Methods. 1996; 69:175–188. [PubMed: 8946321]
70. Bokil H, Andrews P, Kulkarni JE, Mehta S, Mitra PP. Chronux: a platform for analyzing neural signals. J Neurosci Methods. 2010; 192:146–151. [PubMed: 20637804]
71. Smith MA, Jia X, Zandvakili A, Kohn A. Laminar dependence of neuronal correlations in visual cortex. Journal of Neurophysiology. 2013; 109:940–947. [PubMed: 23197461]
72. Mitzdorf U, Singer W. Prominent excitatory pathways in the cat visual cortex (A 17 and A 18): a current source density analysis of electrically evoked potentials. Experimental brain research Experimentelle Hirnforschung Experimentation cerebrale. 1978; 33:371–394.
73. Stoelzel CR, Bereshpolova Y, Swadlow HA. Stability of thalamocortical synaptic transmission across awake brain states. The Journal of neuroscience : the official journal of the Society for Neuroscience. 2009; 29:6851–6859. [PubMed: 19474312]
74. Yazdan-Shahmorad A, Lehmkuhle MJ, Gage GJ, Marzullo TC, Parikh H, Miriani RM, et al. Estimation of electrode location in a rat motor cortex by laminar analysis of electrophysiology and intracortical electrical stimulation. J Neural Eng. 2011; 8:046018. [PubMed: 21690656]
75. Williams JC, Hippensteel JA, Dilgen J, Shain W, Kipke DR. Complex impedance spectroscopy for monitoring tissue responses to inserted neural implants. J Neural Eng. 2007; 4:410–423. [PubMed: 18057508]
76. Moshayedi P, Ng G, Kwok JCF, Yeo GSH, Bryant CE, Fawcett JW, et al. The relationship between glial cell mechanosensitivity and foreign body reactions in the central nervous system. Biomaterials. 2014; 35:3919–3925. [PubMed: 24529901]
77. Prasad A, Xue QS, Dieme R, Sankar V, Mayrand RC, Nishida T, et al. Abiotic-biotic characterization of Pt/Ir microelectrode arrays in chronic implants. Front Neuroeng. 2014; 7:2. [PubMed: 24550823]
78. Kuo JT, Kim BJ, Hara SA, Lee CD, Gutierrez CA, Hoang TQ, et al. Novel flexible Parylene neural probe with 3D sheath structure for enhancing tissue integration. Lab on a Chip. 2013; 13:554–561. [PubMed: 23160191]

79. Kim BJ, Kuo JT, Hara SA, Lee CD, Yu L, Gutierrez CA, et al. 3D Parylene sheath neural probe for chronic recordings. J Neural Eng. 2013; 10:045002. [PubMed: 23723130]
80. McClain MA, Clements IP, Shafer RH, Bellamkonda RV, LaPlaca MC, Allen MG. Highly-compliant, microcable neuroelectrodes fabricated from thin-film gold and PDMS. Biomed Microdevices. 2011; 13:361–373. [PubMed: 21240559]
81. Kozai TDY, Kipke DR. Insertion shuttle with carboxyl terminated self-assembled monolayer coatings for implanting flexible polymer neural probes in the brain. J Neurosci Methods. 2009; 184:199–205. [PubMed: 19666051]
82. Loffler S, Xie Y, Klimach P, Richter A, Detemple P, Stieglitz T, et al. Long term in vivo stability and frequency response of polyimide based flexible array probes. Biomed Tech (Berl). 2012
83. Fan, W.; Maesoon, I.; Euisik, Y. A flexible fish-bone-shaped neural probe strengthened by biodegradable silk coating for enhanced biocompatibility. Solid-State Sensors, Actuators and Microsystems (TRANSDUCERS); 16th IEEE International Conference on; Beijing, China. 2011. p. 966-969.
84. Cheung KC, Renaud P, Tanila H, Djupsund K. Flexible polyimide microelectrode array for in vivo recordings and current source density analysis. Biosens Bioelectron. 2007; 22:1783–1790. [PubMed: 17027251]
85. Kisban S, Herwik S, Seidl K, Rubehn B, Jezzini A, Umilta MA, et al. Microprobe array with low impedance electrodes and highly flexible polyimide cables for acute neural recording. Conf Proc IEEE Eng Med Biol Soc. 2007; 2007:175–178. [PubMed: 18001917]
86. Metz S, Bertsch A, Bertrand D, Renaud P. Flexible polyimide probes with microelectrodes and embedded microfluidic channels for simultaneous drug delivery and multi-channel monitoring of bioelectric activity. Biosensors & Bioelectronics. 2004; 19:1309–1318. [PubMed: 15046764]
87. Rousche PJ, Pellinen DS, Pivin DP Jr, Williams JC, Vetter RJ, Kipke DR. Flexible polyimide-based intracortical electrode arrays with bioactive capability. IEEE Trans Biomed Eng. 2001; 48:361–371. [PubMed: 11327505]
88. Harris JP, Hess AE, Rowan SJ, Weder C, Zorman CA, Tyler DJ, et al. In vivo deployment of mechanically adaptive nanocomposites for intracortical microelectrodes. J Neural Eng. 2011; 8:046010. [PubMed: 21654037]
89. Gilgunn, PJ.; Khilwani, R.; Kozai, TDY.; Weber, DJ.; Cui, XT.; Erdos, G., et al. An ultra-compliant, scalable neural probes with molded biodissolvable delivery vehicle. Micro Electro Mechanical Systems (MEMS); 2012 IEEE 25th International Conference on; 2012. p. 56-59.
90. Ware T, Simon D, Liu C, Musa T, Vasudevan S, Sloan A, et al. Thiol-ene/acrylate substrates for softening intracortical electrodes. J Biomed Mater Res B Appl Biomater. 2014; 102:1–11. [PubMed: 23666562]
91. Lu X, Xu G, Hofstra PG, Bajcar RC. Moisture–absorption, dielectric relaxation, and thermal conductivity studies of polymer composites. Journal of Polymer Science Part B: Polymer Physics. 1998; 36:2259–2265.
92. Hassler C, von Metzen RP, Ruther P, Stieglitz T. Characterization of parylene C as an encapsulation material for implanted neural prostheses. Journal of Biomedical Materials Research Part B: Applied Biomaterials. 2010; 93B:266–274.
93. Hassler, C.; Metzen, R.; Stieglitz, T. Deposition Parameters Determining Insulation Resistance and Crystallinity of Parylene C in Neural Implant Encapsulation. In: Sloten, J.; Verdonck, P.; Nyssen, M.; Haueisen, J., editors. 4th European Conference of the International Federation for Medical and Biological Engineering; Springer Berlin Heidelberg. 2009. p. 2439-2442.
94. Geng J, Zeng T. Influence of single-walled carbon nanotubes induced crystallinity enhancement and morphology change on polymer photovoltaic devices. J Am Chem Soc. 2006; 128:16827–16833. [PubMed: 17177433]
95. Yeh YS, James WJ, Yasuda H. Polymerization of para-xylylene derivatives. VI. morphology of parylene N and parylene C films investigated by gas transport characteristics. Journal of Polymer Science Part B: Polymer Physics. 1990; 28:545–568.
96. Surendran G, Gazicki M, James WJ, Yasuda H. Polymerization of para-xylylene derivatives (parylene polymerization). IV. Effects of the sublimation rate of di-p-xylylene on the morphology

and crystallinity of parylene N deposited at different temperatures. Journal of Polymer Science Part A: Polymer Chemistry. 1987; 25:1481–1503.

97. Surendran G, Gazicki M, James WJ, Yasuda H. Polymerization of para-xylylene derivatives. V. Effects of the sublimation rate of di-p-xylylene on the crystallinity of parylene C deposited at different temperatures. Journal of Polymer Science Part A: Polymer Chemistry. 1987; 25:2089–2106.
98. Fortin, J.; Lu, T. Chemical Vapor Deposition Polymerization: The growth and proerties of parylene thin films. Norwell, Massachusetts: Kluwer Academic Publisher; 2004.
99. Ogurtani TO, Oren EE. Irreversible thermodynamics of triple junctions during the intergranular void motion under the electromigration forces. International Journal of Solids and Structures. 2005; 42:3918–3952.
100. Gottstein G, Shvindlerman LS, Zhao B. Thermodynamics and kinetics of grain boundary triple junctions in metals: Recent developments. Scripta Materialia. 2010; 62:914–917.
101. Ogurtani TO. Mesoscopic nonequilibrium thermodynamics of solid surfaces and interfaces with triple junction singularities under the capillary and electromigration forces in anisotropic three-dimensional space. The Journal of Chemical Physics. 2006; 124
102. Schenk O, Urai JL, Piazolo S. Structure of grain boundaries in wet, synthetic polycrystalline, statically recrystallizing halite – evidence from cryo-SEM observations. Geofluids. 2006; 6:93–104.
103. Schenk O, Urai J. Microstructural evolution and grain boundary structure during static recrystallization in synthetic polycrystals of Sodium Chloride containing saturated brine. Contrib Mineral Petrol. 2004; 146:671–682.
104. Raj R. Creep in polycrystalline aggregates by matter transport through a liquid phase. Journal of Geophysical Research: Solid Earth. 1982; 87:4731–4739.
105. Aveson JW, Reinhart G, Billia B, Nguyen-Thi H, Mangelinck-Noël N, Lafford TA, et al. Observation of the initiation and propagation of solidification cracks by means of in situ synchrotron X-ray radiography. IOP Conference Series: Materials Science and Engineering. 2012; 33:012040.
106. Weinan, E. Principles of Multiscale Modeling. Cambridge: Cambridge University Press; 2011.
107. Kim, BJ.; Washabaugh, EP.; Meng, E. Annealing effects on flexible multi-layered parylene-based sensors. Micro Electro Mechanical Systems (MEMS); 2014 IEEE 27th International Conference on; 2014. p. 825-828.
108. Seymour JP, Elkasabi YM, Chen HY, Lahann J, Kipke DR. The insulation performance of reactive parylene films in implantable electronic devices. Biomaterials. 2009; 30:6158–6167. [PubMed: 19703712]
109. Franssila, S. Introduction to Microfabrication. Chichester, West Sussex (UK): John Wiley & Sons, Ltd; 2010.
110. Ludwig KA, Langhals NB, Joseph MD, Richardson-Burns SM, Hendricks JL, Kipke DR. Poly(3,4-ethylenedioxythiophene) (PEDOT) polymer coatings facilitate smaller neural recording electrodes. J Neural Eng. 2011; 8:014001. [PubMed: 21245527]
111. Purcell EK, Thompson DE, Ludwig KA, Kipke DR. Flavopiridol reduces the impedance of neural prostheses in vivo without affecting recording quality. J Neurosci Methods. 2009; 183:149–157. [PubMed: 19560490]
112. Ludwig KA, Uram JD, Yang J, Martin DC, Kipke DR. Chronic neural recordings using silicon microelectrode arrays electrochemically deposited with a poly(3,4-ethylenedioxythiophene) (PEDOT) film. J Neural Eng. 2006; 3:59–70. [PubMed: 16510943]
113. Vetter RJ, Williams JC, Hetke JF, Nunamaker EA, Kipke DR. Chronic neural recording using silicon-substrate microelectrode arrays implanted in cerebral cortex. IEEE Trans Biomed Eng. 2004; 51:896–904. [PubMed: 15188856]
114. Griffith RW, Humphrey DR. Long-term gliosis around chronically implanted platinum electrodes in the Rhesus macaque motor cortex. Neurosci Lett. 2006; 406:81–86. [PubMed: 16905255]
115. Turner JN, Shain W, Szarowski DH, Andersen M, Martins S, Isaacson M, et al. Cerebral astrocyte response to micromachined silicon implants. Exp Neurol. 1999; 156:33–49. [PubMed: 10192775]

116. Nieuwenhuys, R.; Ten Donkelaar, HJ.; Nicholson, C. The Central Nervous System of Vertebrates. Berlin: Springer; 1998.
117. Rehkamper G, Frahm HD, Zilles K. Quantitative development of brain and brain structures in birds (galliformes and passeriformes) compared to that in mammals (insectivores and primates). Brain Behav Evol. 1991; 37:125–143. [PubMed: 2070254]
118. Elias MF. Relative maturity of cebus and squirrel monkeys at birth and during infancy. Dev Psychobiol. 1977; 10:519–528. [PubMed: 413756]
119. Roth G, Dicke U. Evolution of the brain and intelligence in primates. Prog Brain Res. 2012; 195:413–430. [PubMed: 22230639]
120. Roth G, Dicke U. Evolution of the brain and intelligence. Trends Cogn Sci. 2005; 9:250–257. [PubMed: 15866152]
121. Blinkov, SM.; Glezer, II. A Quantitative Handbook. New York: Plenum Press; 1968. The Human Brain in Figures and Tables.
122. Seymour JP, Kipke DR. Neural probe design for reduced tissue encapsulation in CNS. Biomaterials. 2007; 28:3594–3607. [PubMed: 17517431]
123. Skousen JL, Merriam SM, Srivannavit O, Perlin G, Wise KD, Tresco PA. Reducing surface area while maintaining implant penetrating profile lowers the brain foreign body response to chronically implanted planar silicon microelectrode arrays. Prog Brain Res. 2011; 194:167–180. [PubMed: 21867802]
124. Guitchounts G, Markowitz JE, Liberti WA, Gardner TJ. A carbon-fiber electrode array for long-term neural recording. J Neural Eng. 2013; 10:046016. [PubMed: 23860226]
125. Bai YX, Ho SS, Kotov NA. Direct-write maskless lithography of LBL nanocomposite films and its prospects for MEMS technologies. Nanoscale. 2012; 4:4393–4398. [PubMed: 22740054]
126. Shim BS, Zhu J, Jan E, Critchley K, Kotov NA. Transparent conductors from layer-by-layer assembled SWNT films: importance of mechanical properties and a new figure of merit. ACS Nano. 2010; 4:3725–3734. [PubMed: 20552974]
127. Shim BS, Zhu J, Jan E, Critchley K, Ho S, Podsiadlo P, et al. Multiparameter Structural Optimization of Single-Walled Carbon Nanotube Composites: Toward Record Strength, Stiffness, and Toughness. ACS Nano. 2009
128. Jan E, Hendricks JL, Husaini V, Richardson-Burns SM, Sereno A, Martin DC, et al. Layered carbon nanotube-polyelectrolyte electrodes outperform traditional neural interface materials. Nano Lett. 2009; 9:4012–4018. [PubMed: 19785391]
129. Shim BS, Chen W, Doty C, Xu C, Kotov NA. Smart electronic yarns and wearable fabrics for human biomonitoring made by carbon nanotube coating with polyelectrolytes. Nano Lett. 2008; 8:4151–4157. [PubMed: 19367926]
130. Zhang H, Patel PR, Xie Z, Swanson SD, Wang X, Kotov NA. Tissue-compliant neural implants from microfabricated carbon nanotube multilayer composite. ACS Nano. 2013; 7:7619–7629. [PubMed: 23930825]
131. Skorb EV, Andreeva DV. Layer-by-Layer approaches for formation of smart self-healing materials. Polymer Chemistry. 2013; 4:4834–4845.
132. Yoshida M, Lahann J. Smart nanomaterials. ACS Nano. 2008; 2:1101–1107. [PubMed: 19206325]
133. Nandivada H, Chen HY, Bondarenko L, Lahann J. Reactive polymer coatings that "Click". Angew Chem Int Ed Engl. 2006; 45:3360–3363. [PubMed: 16622893]
134. Lahann J. Vapor-based polymer coatings for potential biomedical applications. Polym Int. 2006; 55:1361–1370.
135. Elkasabi Y, Chen HY, Lahann J. Multipotent polymer coatings based on chemical vapor deposition copolymerization. Adv Mater. 2006; 18:1521.
136. Lahann J, Chen HY. Preparation of non-fouling coatings made by chemical vapor deposition polymerization. Abstr Pap Am Chem S. 2005; 230:U4292–U4293.
137. Lahann J. Bio-functional polymer coatings based on chemical vapor deposition. Abstr Pap Am Chem S. 2005; 229:U1106-U.

138. Lahann J, Balcells M, Lu H, Rodon T, Jensen KF, Langer R. Reactive polymer coatings: a first step toward surface engineering of microfluidic devices. Anal Chem. 2003; 75:2117–2122. [PubMed: 12720350]

139. Lahann J, Mitragotri S, Tran TN, Kaido H, Sundaram J, Choi IS, et al. A reversibly switching surface. Science. 2003; 299:371–374. [PubMed: 12532011]

140. Lahann J, Hocker H, Langer R. Synthesis of Amino[2.2]paracyclophanes-Beneficial Monomers for Bioactive Coating of Medical Implant Materials. Angew Chem Int Ed Engl. 2001; 40:2947. [PubMed: 12203613]

141. Lahann J, Klee D, Pluester W, Hoecker H. Bioactive immobilization of r-hirudin on CVD-coated metallic implant devices. Biomaterials. 2001; 22:817–826. [PubMed: 11246950]

142. Lahann J, Choi IS, Lee J, Jenson KF, Langer R. A new method toward microengineered surfaces based on reactive coating. Angew Chem Int Edit. 2001; 40:3166.

143. Bally F, Cheng K, Nandivada H, Deng X, Ross AM, Panades A, et al. Co-immobilization of biomolecules on ultrathin reactive chemical vapor deposition coatings using multiple click chemistry strategies. ACS Appl Mater Interfaces. 2013; 5:9262–9268. [PubMed: 23888837]

144. Deng X, Eyster TW, Elkasabi Y, Lahann J. Bio-orthogonal polymer coatings for co-presentation of biomolecules. Macromol Rapid Commun. 2012; 33:640–645. [PubMed: 22351186]

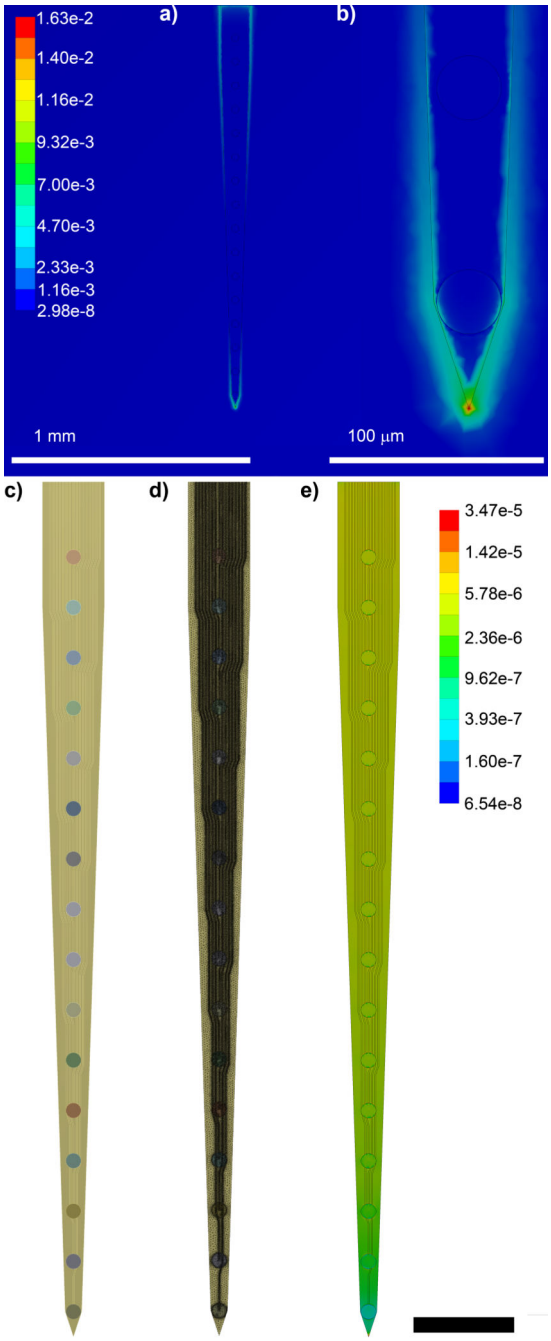

Figure 1.

Finite Element Modeling of Von Mises's Equivalent Strain. **a)** Brain tissue strain surrounding an implanted electrode subject to a 1 μm displacement in the planar direction. **b)** Zoomed in feature of (a) showing peak strain at the tip of the electrode. **c)** FEM of 16 channel single shank planar silicon electrode. **d)** Assembled mesh of (c). **e)** Von Mises Equivalent Elastic Strain (μm/μm) of (c) when a 1 μm displacement is applied at the tip in the vector normal to the planar surface. Scale bar = 200 μm.

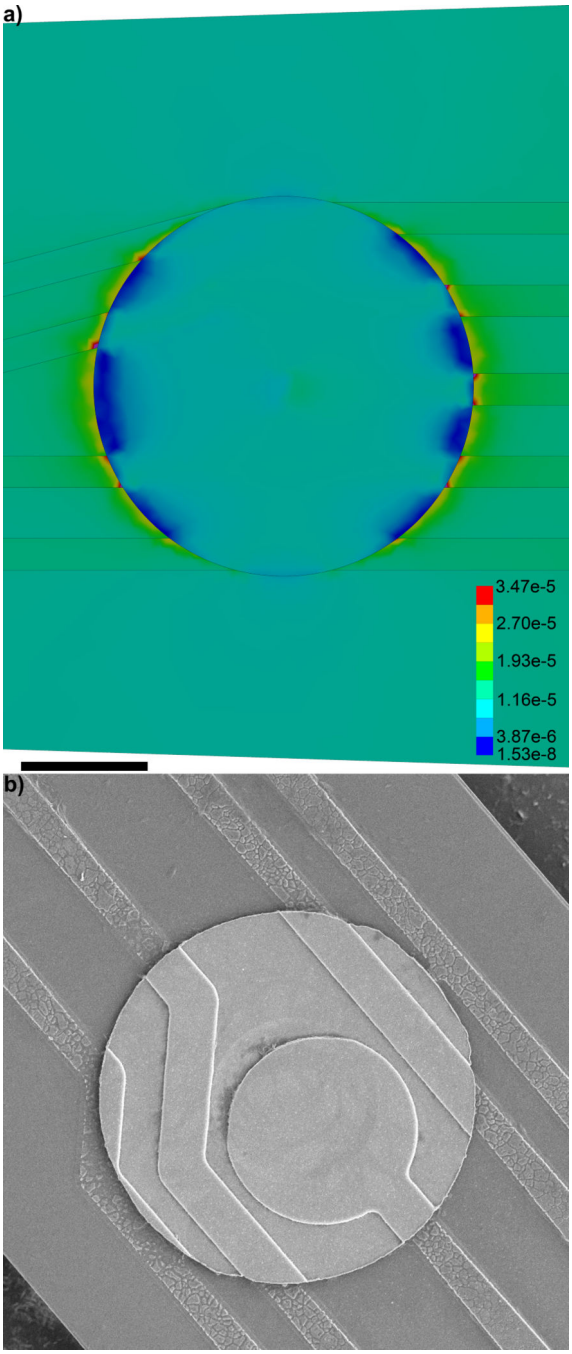

Figure 2.

Von Mises Equivalent Elastic Strain (μm/μm) distribution around the 5th electrode in the model 16 channel single shank planar silicon electrode. **a)** Note the strain is highest around the edges of electrode trace next to the edge of the iridium recording site. **b)** Cracking and degradation of the traces around the recording site can be observed in the SEM. Scale bar = 10 μm.

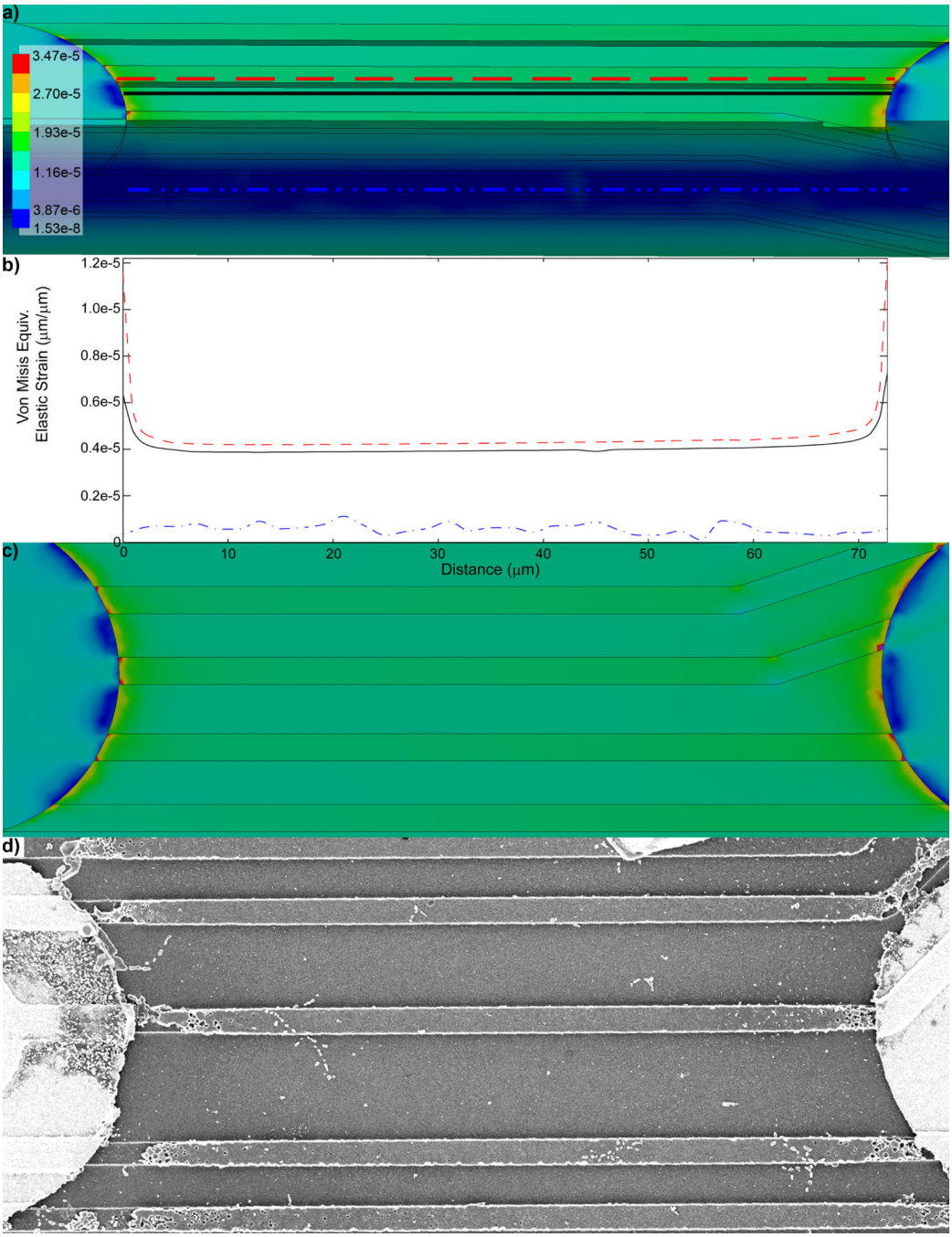

Figure 3.

Von Mises Equivalent Elastic Strain (µm/µm) between recording sites. **a)** Strain distribution in a cross-section of the probe. The strain is the lowest in the interior of the probe and greatest on the protruding traces. Scale bar = 100 µm. Red dashed line, black solid line, and blue dash done line indicate the location in which strain was measured for (b). **b)** Von Mises Equivalent Elastic Strain (µm/µm) between the 5th and 6th recording sites; at the surface of the electrical trace structure (red dashed line), at the surface of the substrate next to a trace (black solid line), and inside probe at the middle of the substrate (blue dash dot line). **c)** Von

Mises Equivalent Elastic Strain (μm/μm). **d)** SEM of a trace between the 5th and 6th recording site of a probe explanted 189 days after implantation shows structural degradation and fracturing of protruding traces near the edges of the iridium recording sites (Fig. S4).

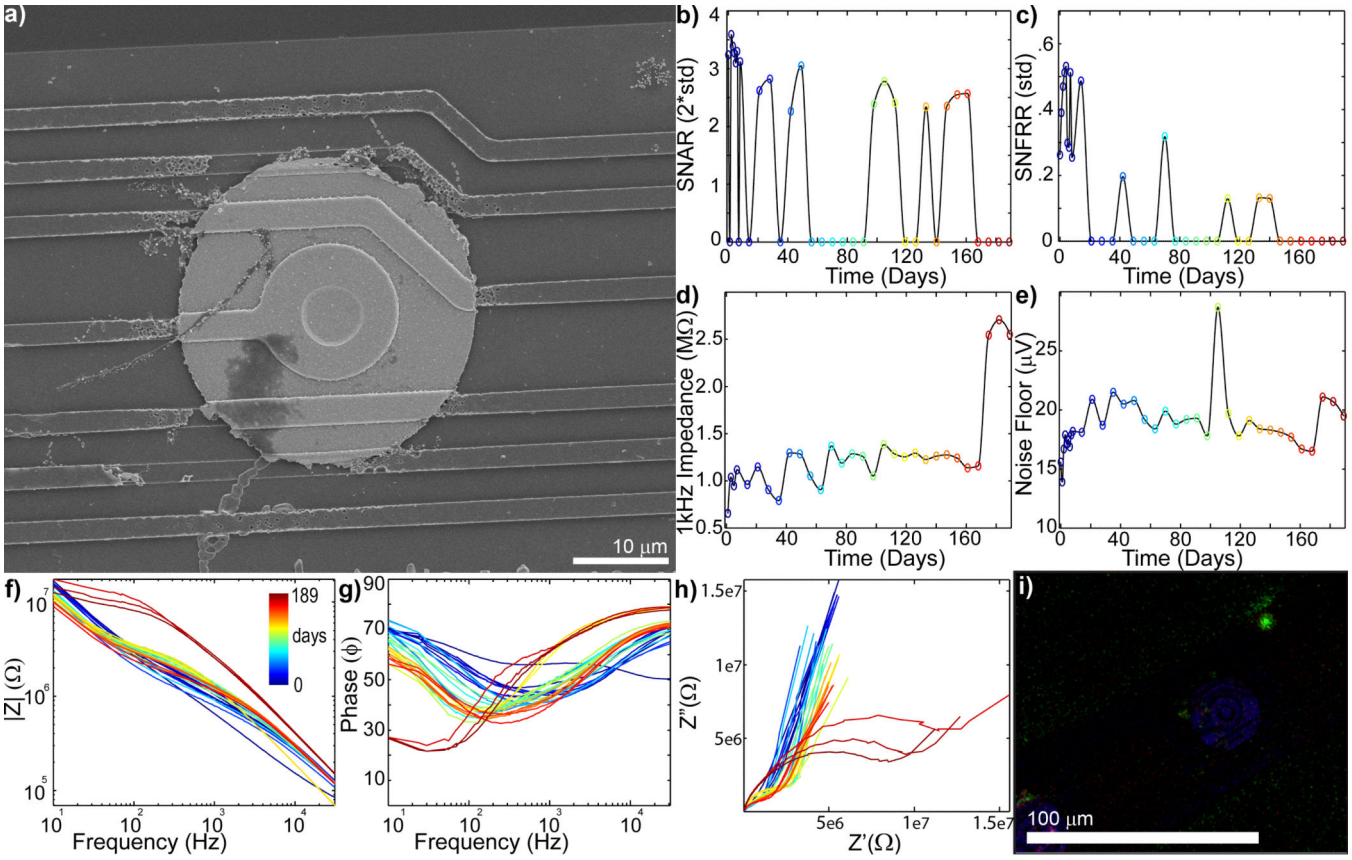

Figure 4.

Chronic *in vivo* electrode failure can cause an increase in impedance (day 0 = blue to day 189 = red: recording site #7 of Fig S4). **a)** SEM of recording site shows complete trace degradation around the recording site (see Fig. S5 for close up). SU SNAR (b) and MU SNFRR (c) show spike recording disappears around day 168. 1kHz Impedance (d) and noise floor (e) shows abrupt increase on day 175. **f)** Bode Magnitude (|Z|) shows large increase in impedance across all frequencies on day 175. **g)** Bode Phase (Phase) shows dramatic shift on day 175. **h)** Nyquist (Z' vs Z") plot shows a large increase in the RC component and lower tail starting on day 175. **I)** Immunohistochemistry [Iba1 (Green), Vimentin (Red), IgG (Blue), Hoechst (White)] shows limited glial adhesion. The Iba1 positive biological fragment over the degraded traces further supports recording and impedance data indicating that the mechanical failure occurred *in vivo*.

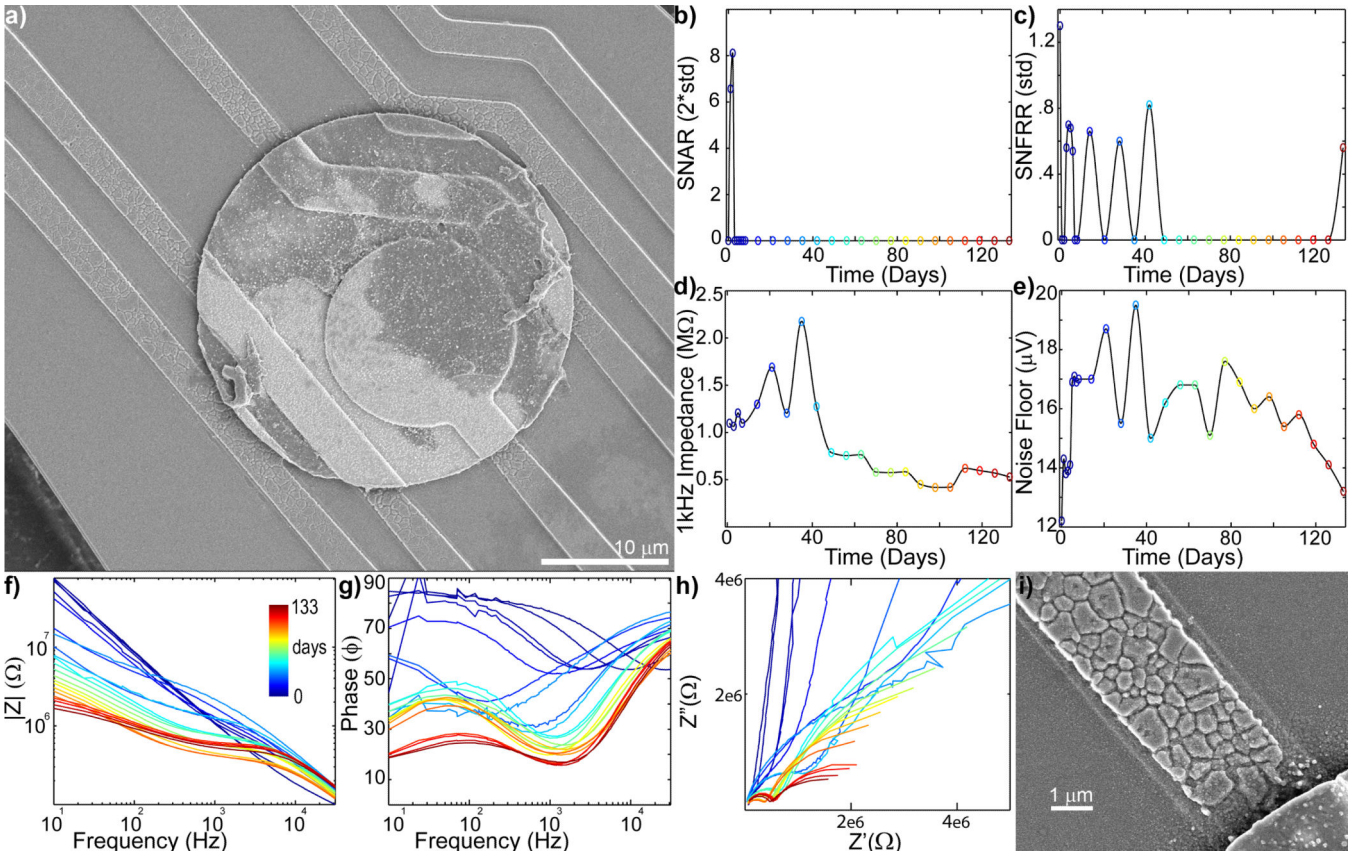

Figure 5.

b) Chronic *in vivo* electrode failure can cause a decrease in impedance (day 0 = blue to day 133 = red: recording site #6 of Fig S1). **a)** SEM shows degradation of the electrical trace around the edge of the recording site. Drop in SU SNAR (b) and MU SNFRR (c) recording coincides with the large jump in impedance (d) on day 35, followed by a large drop starting on day 42. Dramatic shifts in Bode Magnitude (f), Bode Phase (g), and Nyquist (h) plots can also be observed at this time point. Noisy (jagged) curves in the Bode Phase and Nyquist plot on day 35 indicates a break in the electrical circuit. The subsequent smooth curves suggest the remaining intact electrical trace became de-insulated. **i)** Zoomed in SEM of eroded electrical trace.

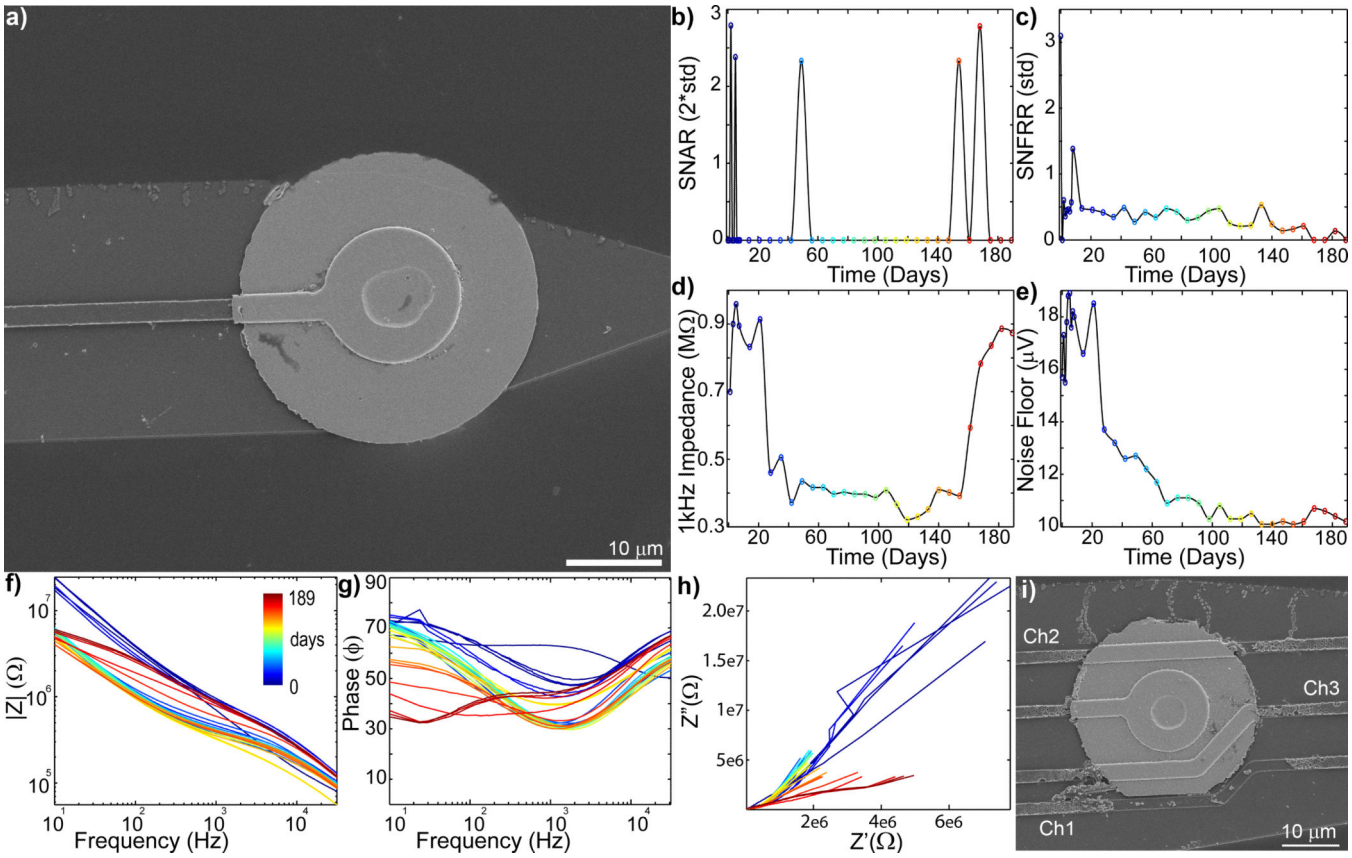

Figure 6.

Complex chronic *in vivo* electrode failure when the trace around the recording site is intact. (day 0 = blue to day 189 = red: recording site #1 of Fig. S4). **a)** SEM of recording site #1 shows the trace is intact. **b)** SU SNAR is limited between days 14 and 147. **c)** MU SNFRR shows significant (p>0.05) evoked activity until day 168. **d)** Impedance dramatically drops between days 14 to 28 then dramatically increases between days 154 to 168. **e)** Noise floor largely drops between days 14 to 28, then slow decreases until day 98, and then slightly increases on day 168. **f)** Body Magnitude (|Z|) plot shows only the high frequency impedance drop on day 14. That is followed by a decrease in impedance across all frequencies, and then and increase in impedance across all frequencies starting on day 175. **g)** Similarly, large shifts in the Bode Phase plot can been observed on day 14 and day 175. **h)** Nyquist plot (Z' vs Z") shows a dramatic decrease in reactance (Z") and resistance (Z') on day 14, then an increase in resistance from day 147 to 175. **i)** SEM of recording site #4 shows degradation of the electrical trace from recording site #1.

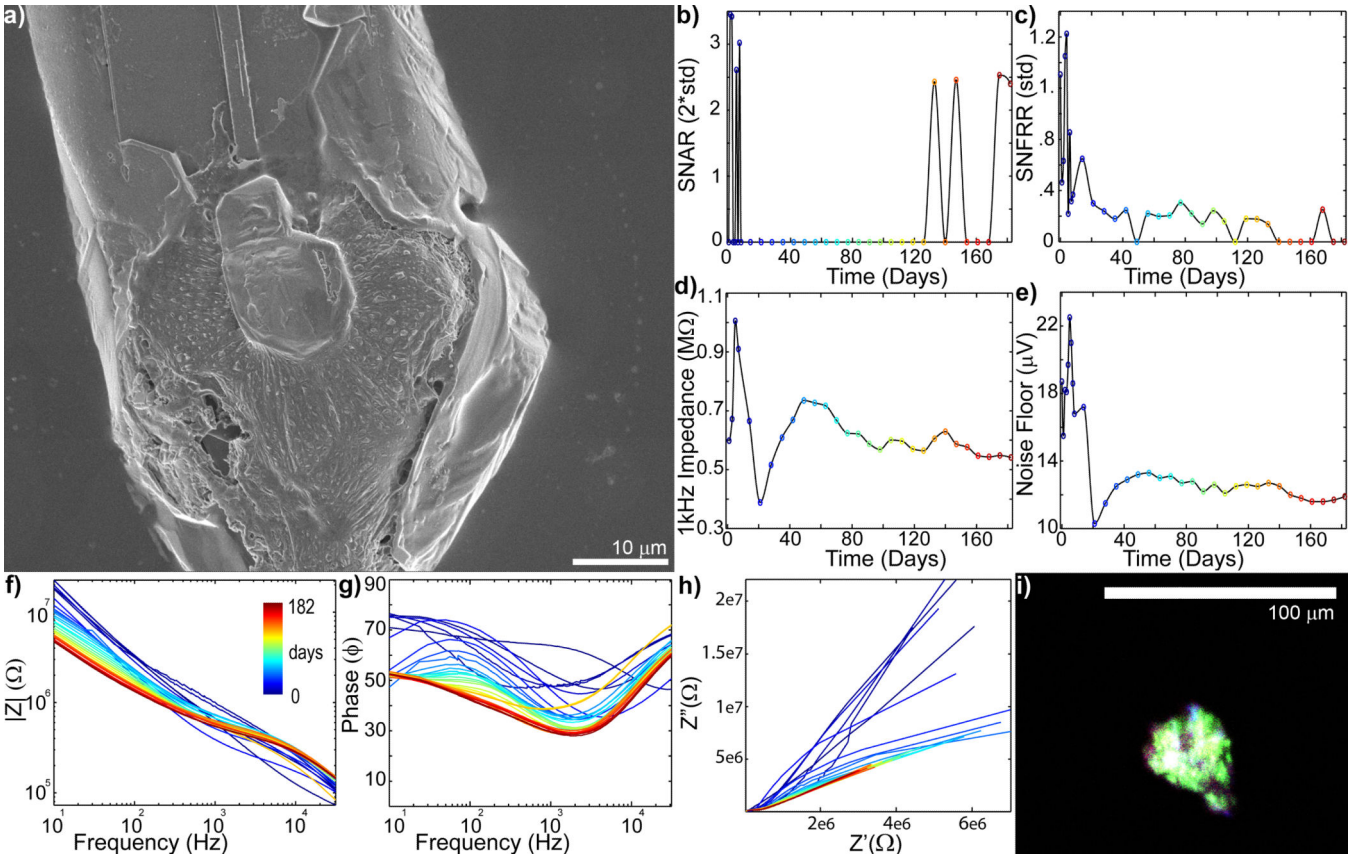

Figure 7.

Complex chronic *in vivo* electrode failure and low level recovery when electrode failure is accompanied by glial encapsulation (day 0 = blue to day 182 = red: recording site #1 of Fig S2). **a)** SEM of recording site shows substantial cellular encapsulation. **b)** SU SNAR is lost after the first week, but sporadically returns starting on day 126. **c)** MU SNFRR dramatically decreases after the first week, and then degrades around day 133–140. **d)** 1kHz Impedance greatly increases over the first week, then drops over the following two weeks. It then gradually increases between days 28 to 49, and then slowly decreases over the remainder of the implant period. **e)** Noise Floor, similarly, increases over the first week, and drops between days 7 and 21. This is followed by a gradual increase between days 28 to 49. **f)** Bode Magnitude (|Z|) shows only the higher frequencies (>200 Hz) increased on day 5 and 7 and decreased on day 8. This was followed by a decrease across most frequencies (<4 kHz) on day 14. Impedance recovered between day 28 and 49, then preferentially decreased over the lower frequencies over the remaining implant period. **g)** Bode Phase (Phase) shows large changes over the first 7 weeks, followed by a slow resistive shift. **h)** Nyquist (Z' vs Z") plot shows limited RC (charge transfer) arc typically expected from glial encapsulated recording sites. **i)** Immunohistochemistry [Iba1 (Green), Vimentin (Red), IgG (Blue), Hoechst (White)] shows that the cellular encapsulation is glial. A complex relationship between gliosis and insulation failure may lead to low level functionality. Glial encapsulation occurring with trace de-insulation failure may be difficult to identify from Bode and Nyquist plots alone.

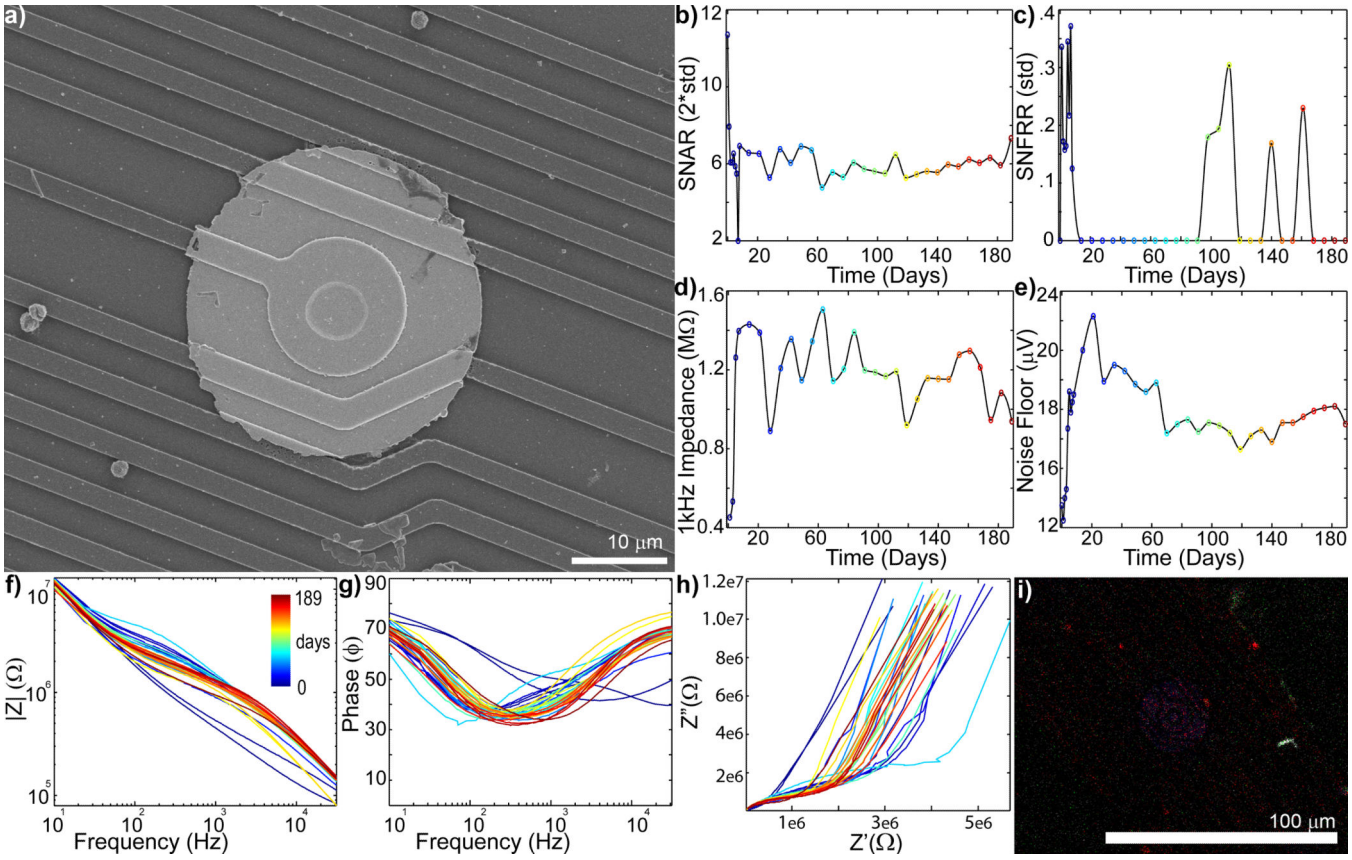

Figure 8.

Recording sites with good recording performance show limited material failure (day 0 = blue to day 189 = red: recording site #12 of Fig. S4). **a)** SEM of recording sites showing good material stability. Careful examination of the traces around the edge of the Ir electrode shows small perforations in the insulation. **b)** SU SNAR shows robust single-unit activity over the duration of the implant. **c)** MU SNFRR shows some evoked activit. **d)** 1kHz Impedance increases over the first week, but is largely stable. **e)** Noise floor also shows gradual increase over the first week, but is mostly stable thereafter. **f)** Bode Magnitude(|Z|) shows an increase over the first week, but is stable after that. **g)** Bode Phase (Phase) shows mostly a decrease over the first week, but does not substantially change afterward. **h)** Nyquist (Z' vs Z") plot shows some shift over time, but the tail slope remains mostly the same. **i)** Immunohistochemistry [Iba1 (Green), Vimentin (Red), IgG (Blue), Hoechst (White)] shows no glial adhesion and limited vimentin labeling

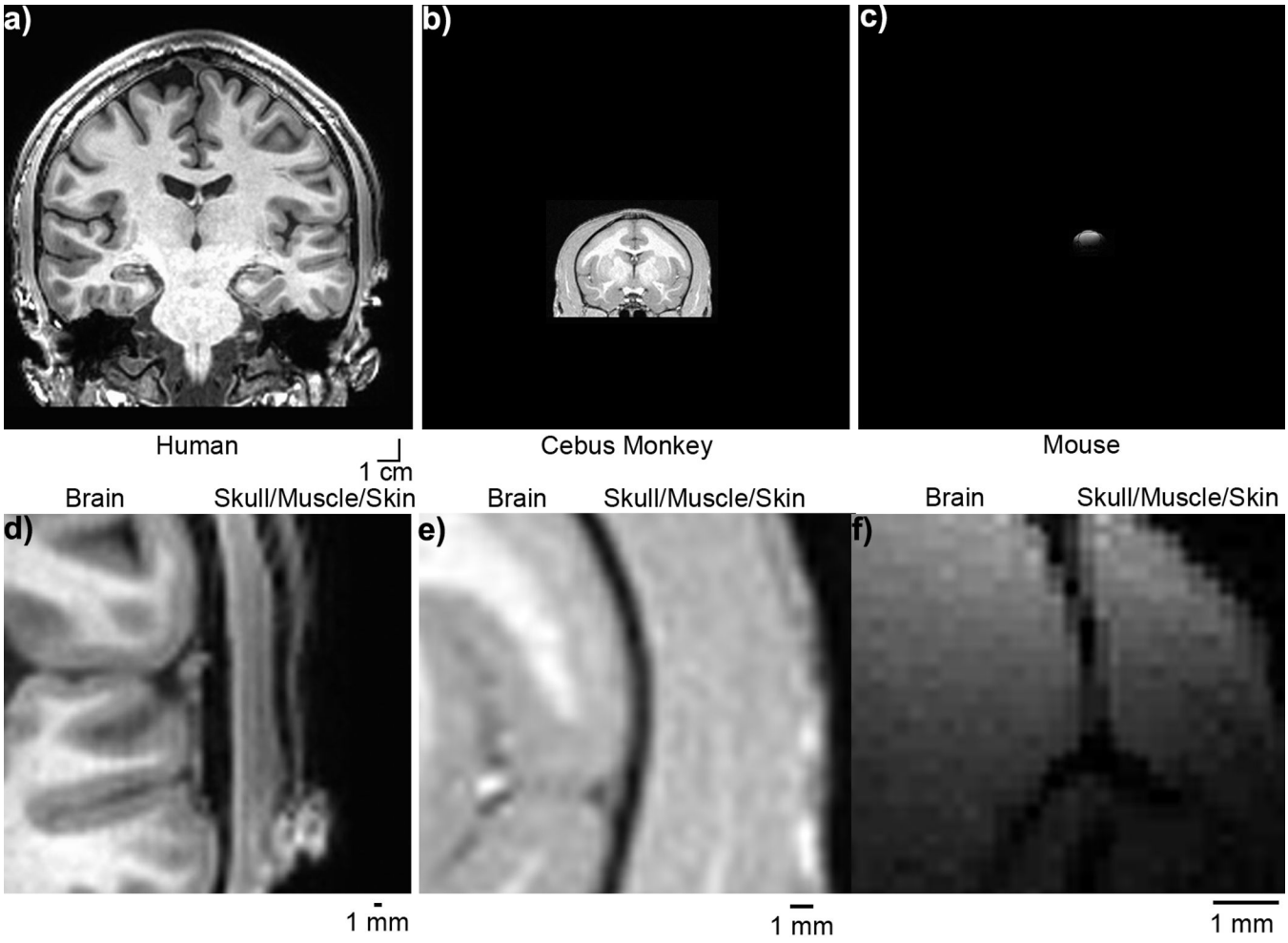

Figure 9.

Brain Size Figure. Human (a), Cebus Monkey (b), and Mouse (c) brain and skull on the same 1cm scale bar. Zoomed in image showing interstitial space between Human (d), Cebus Monkey (e),and Mouse (f). Scale bar = 1 mm. Note: (a–c) have the same scale bar, while (d–f) have different scale bars.

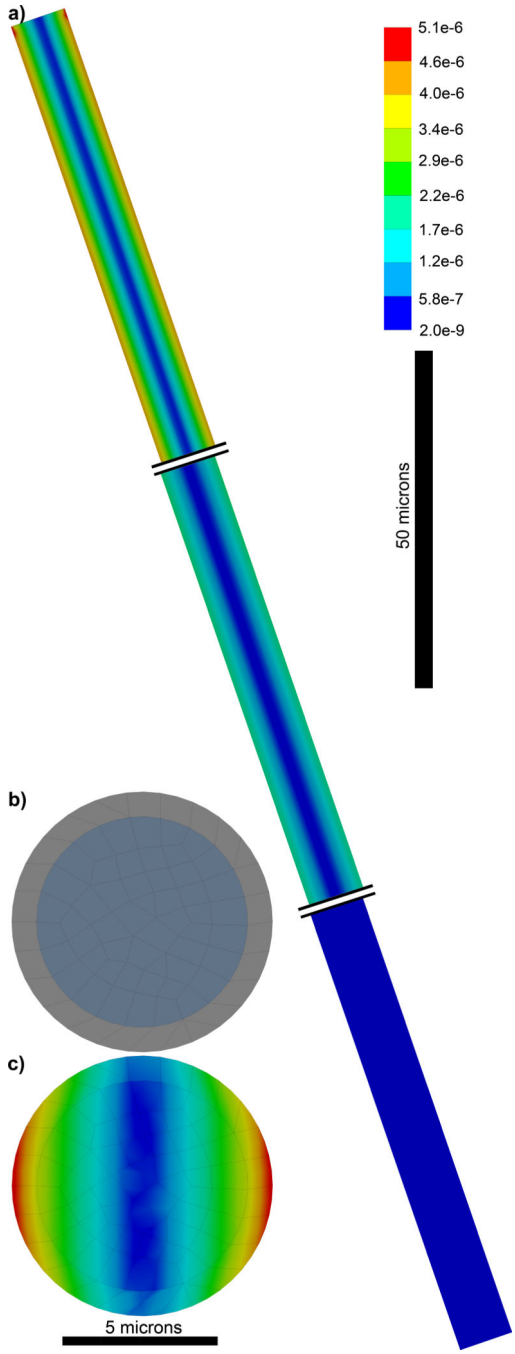

Figure 10.

FEM of a carbon fiber Microthread Electrode. **a)** 1.65 mm long fixed at the top and with a recording site on the bottom. Double lines are shown truncating the fiber so the strain can be observed along the base, center, and tip of the fiber. **b)** Cross-section of the Microthread electrode showing the carbon fiber core and parylene insulation. **c)** Von Mises Equivalent Elastic Strain long the cross-section of the electrode 1 micron from the base showing a more evenly distributed strain.